Universidade de São Paulo
Instituto de Astronomia, Geofísica e Ciências Atmosféricas
Departamento de Astronomia

Douglas Ferreira Carlos

γ-rays from AGN in dwarf galaxies

São Paulo
2022

Douglas Ferreira Carlos

γ-rays from AGN in dwarf galaxies

Dissertation submitted to the Institute of Astronomy, Geophysics and Atmospheric Sciences of the University of São Paulo as partial fulfillment of the requirements for the degree of Master of Science.

Area: Astronomy

Advisor: Prof. Dr. Rodrigo Nemmen da Silva

São Paulo

2022

Este trabalho é dedicado a todos os educadores que, através da profissão ou da amizade, me ensinaram novas formas de enxergar o mundo.

Agradecimentos / Acknowledgements

Agradeço à minha família pelo apoio e carinho que sempre me deram;

Agradeço aos meus amigos pelos momentos de alegria que nunca me fugirão da memória;

Agradeço aos professores que me iluminaram o caminho;

E agradeço à FAPESP pelo apoio financeiro sob o projeto n^o: 2020/10211-2, sem o qual este trabalho não poderia ter sido realizado.

Esta tese foi escrita em LaTeX com a classe IAGTESE, para teses e dissertações do IAG.

"*Há uma teoria que diz que se alguém descobrir exatamente o que é o Universo e seu motivo de existir, ele desaparecerá instantâneamente e será substituído por algo ainda mais bizarro e inexplicável.*

Há uma outra teoria que afirma que isso já aconteceu."

Douglas Adams, O Restaurante no Fim do Universo

Resumo

Entender a física e demografias dos buracos negros (BHs) no regime de massa intermediária pode nos levar a um melhor entendimento dos processos de feedback de AGN, co-evolução galáxia-BH, e até iluminar os mecanismos que formaram as sementes dos buracos negros supermassivos de hoje em dia. Uma abordagem promissora para aprender sobre a atividade dos BHs de massa intermediária é a busca por sua emissão de altas energias em galáxias anãs locais. Neste trabalho, utilizamos 13 anos de dados do Large Area Telescope (LAT) a bordo da espaçonave *Fermi* e implementamos uma técnica de stacking para procurar pelos raios-γ de uma população de 135 galáxias anãs que exibem assinaturas de AGN em diferentes partes do espectro eletromagnético. Com nosso método de stacking, encontramos emissão significativa vinda desta população, mesmo que a maioria dos objetos sejam fracos demais para serem detectados individualmente. Duas das galáxias alvo são fortes candidatos a fontes de raios-γ, exibindo excessos de $\sim 4\sigma$ cada um e luminosidades da ordem de $L_\gamma \sim 10^{42}$ erg/s. Nós exploramos possíveis correlações envolvendo as luminosidades de nossa população de AGN em anãs, e encontramos que os candidatos mais fortes exibem luminosidades em raios-γ acima do esperado a partir das taxas de formação estelar observadas de suas galáxias, o que sugere que a contribuição do AGN para esta banda está superando a de processos estelares típicos. Os altos valores de L_γ para os melhores candidatos levanta a possibilidade de que sua emissão origina em jatos relativísticos até então não detectados.

Abstract

Understanding the physics and demographics of black holes (BHs) in the intermediate-mass regime can lead us to a better understanding of the processes of AGN feedback, BH-galaxy co-evolution, and even shed light on the mechanisms that formed the seeds of today's supermassive black holes. A promising approach to learn about the activity of the elusive intermediate-mass BHs is to look for their high energy emission in nearby dwarf galaxies. In this work we used 13 years of data from the Large Area Telescope (LAT) aboard the Fermi spacecraft and implemented a stacking analysis to look for possible γ-rays from a 135 dwarf galaxies exhibiting signatures of AGN activity in different parts of the electromagnetic spectrum. With our stacking technique, we find that dwarf AGN as a population are significant γ-ray emitters even though most objects are individually too faint. Two of our target galaxies constitute strong candidates for γ-ray sources, both exhibiting $\sim 4\sigma$ excesses and luminosities of up to $L_\gamma \sim 10^{42}$ erg/s. We explore possible correlations involving the luminosities of our dwarf AGN population and find the two strongest candidates are too bright when compared to the γ-ray activity expected from their host galaxy's star formation rates, suggesting the AGN contribution to this band is surpassing that of typical stellar processes. The large values of L_γ for the best candidates also raises the possibility that their emission has its origin in hitherto undetected relativistic jets.

Contents

Chapter 1

Introduction

Astronomers have long been preoccupied in figuring out all the relevant processes responsible for shaping galaxies. At least since the last half of the 18th century, when Thomas Wright and Immanuel Kant first proposed some of the "faint nebulae" in the sky to actually be other island universes all onto themselves, just like the Milky Way.

In their effort, astronomers have employed the use of many tools developed by other scientific disciplines, from basic gravitation and chemistry to quantum mechanics and computer simulations, and have arrived at a hierarchical picture for the formation of large-scale structure in the Universe that sees dwarf galaxies as the building blocks of greater systems. If this is the case, the local dwarf galaxies that remain undevoured may be thought of as relics from that initial phase of assembly, offering us laboratories to study the mechanisms that operated far back when the first galaxies were forming.

One ingredient whose importance for shaping massive galaxies is widely recognized nowadays are the supermassive black holes (SMBHs) of active galactic nuclei (AGN). The exact ways in which SMBHs affect their surroundings is still not well understood, but there are hints that their activity can heat up or outright expel gas from their host's interstellar medium (ISM), slowing down or potentially ceasing the formation of new stars. It is possible that the effects of black hole activity would be even more relevant in the low-mass environments of dwarf galaxies.

Although very recent, searches for AGN in such systems have already identified a couple hundreds of candidates by looking for different signatures of accretion onto black holes; a few of which have mass estimates which places them on the intermediate-mass regime between $10^2 - 10^5 M_\odot$. Since black hole activity is often associated with high energy pro-

cesses capable of accelerating particles to relativistic speeds, these dwarf AGN may end up converting a fraction of the energy released during accretion into γ-rays. And so by studying this high energy messengers we may learn more about the physics operating in the low-mass end of both black hole and galaxy populations.

In the present work we employ the observations of the *Fermi* Large Area Telescope (LAT) and try to answer the question of whether the AGN of dwarf galaxies are γ-ray emitters.

We start by going over a few basic properties of dwarf galaxies and how they relate to more massive ones, then we contextualize their importance for modern cosmology and move on to introduce the relevant literature dedicated to searching for signs of black holes in these systems. By the end of this chapter we will also discuss some of the high energy processes associated with the SMBHs and the instrument we use in our investigation.

1.1 Dwarf galaxies

Historically, the definition used to separate dwarf galaxies from their more massive counterparts has been based in easy to measure properties like size and brightness. At a conference held in the Observatoire de Haute-Provence in 1993, the use of the term dwarf galaxy was agreed to apply for objects that had $M_B \geq -16$ (Hodge, 1971; Tammann, 1994). In addition, later studies on the kinematics of these objects have revealed how dwarfs sit inside dark matter halos just like larger galaxies (Mateo, 1998); this characteristic makes them distinct from globular clusters (GCs), which are usually smaller and do not contain any dark matter.

However, it was pointed out in Tolstoy et al. (2009) how the $M_B \geq -16$ criteria was more of a practical than a physical separation, since all galaxies show continuous relations in structural, kinematic and population features between the biggest and the smallest of their type.

Dwarf galaxies can be divided into the following classes: dwarf ellipticals (dE) contain old Population II stars, little to no gas and dust, and low surface brightness. They are commonly found in groups or clusters of galaxies. The dwarf spheroidals (dS) are similar to the dEs but less bright and as the name suggests, have a more round shape. Dwarf

irregulars (dI or dIrr) contain at least a few Population I stars as well as a considerable amount of gas, with their irregular shape likely attributable to a recent tidal disruption or merger event. There are also late-type dwarfs, in general bluer and richer in gas than the previous ones, and whose stars have organized in a disk with or without spiral arms (Schombert et al., 1995). The ultra-compact dwarfs (UCD) have small sizes comparable to GCs, but are identified as galaxies by their spectra; these are believed to be the stripped nucleus of previously larger dwarf galaxies (Drinkwater et al., 2003). Another interesting class are the ultra-faint dwarfs (uFd), with $L_{\rm tot} \lesssim 10^5 L_\odot$ they have been identified as the faintest and most dark-matter dominated members of the local group (Kirby et al., 2008; Martin et al., 2008); their extremely low surface brightnesses ($\mu_V > 26$ mag arcsec^{-2}, see Figure 1.1) makes uFds very diffuse, which some authors say could be due to intense episodes of gas-loss that may have happened early in their history van Dokkum et al. (2015).

To help illustrate how dwarf galaxies compare with other types of objects we refer to Figure 1.1 from the review of Tolstoy et al. (2009). In both plots we see emerge some sort of main sequence that appears to connects dwarfs galaxies (including uFds) to the more massive ellipticals along a straight line while keeping globular clusters well separated in the $\rm M_V - \mu_V$ plane. This relation is unchanged over a range of ~ 15 magnitudes in M_V which suggests dwarf galaxies represent the extension of normal galaxies to lower masses (and brightness) with no real discontinuity between them, at the same time that it reinforces the separation between dwarfs and globular clusters. Furthermore, the overlap between early and late-type dwarfs has been shown as evidence that early-type dwarfs are the same as late-type systems that have lost their gas (Kormendy, 1985).

Another important aspect of dwarf galaxies to keep in mind is their low metallicities. In fact, the relation involving the mass and metallicity of galaxies shows a rapid transition takes place between low-mass metal-poor systems to higher-mass metal-rich around $3 \times 10^9 M_\odot \lesssim M_* \lesssim 3 \times 10^{10} M_\odot$ (Tremonti et al., 2004; Gallazzi et al., 2005). These extremely low metallicities are hard to reconcile with the observations that most field dwarfs are actively forming stars, and so it has been suggested that processes related to star formation (SF) such as supernova winds might be more effective at expelling gas from these lower-mass systems (Larson, 1974; Matteucci and Chiosi, 1983; Geha et al., 2012; Caproni et al., 2015, 2017).

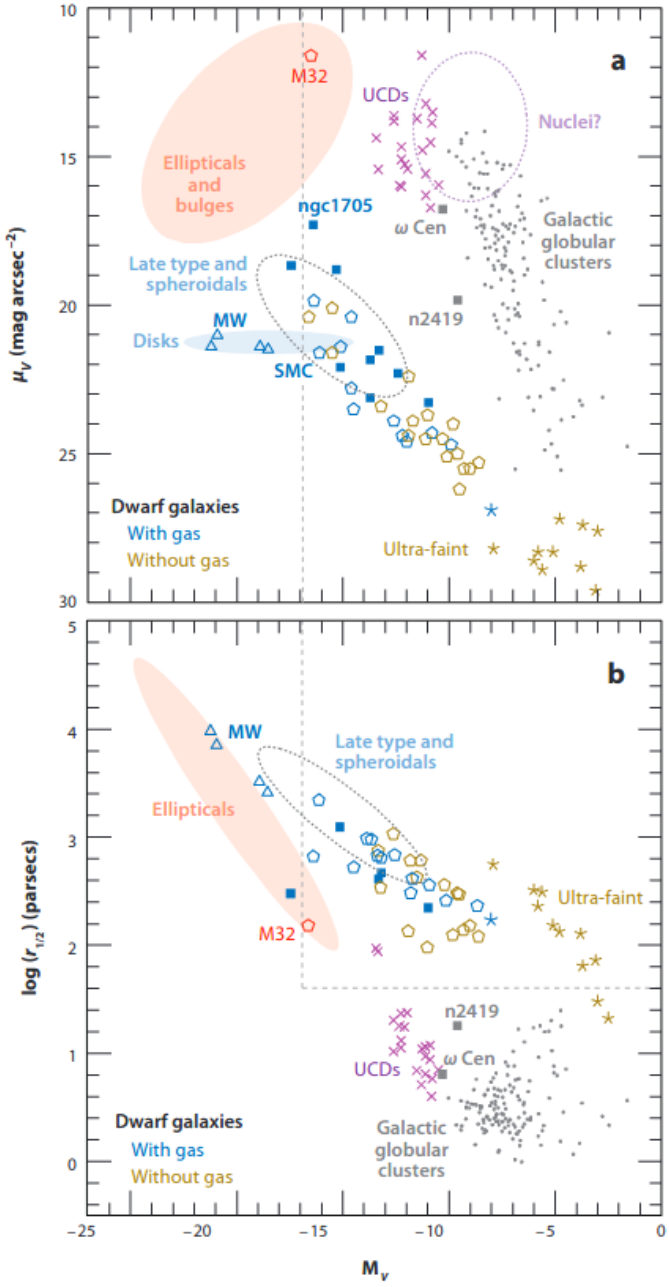

Figure 1.1: Plot displaying the relationship between structural properties of different types of galaxies from Tolstoy et al. (2009). (a) Nuclear surface brightness μ_V and (b) half-light radius $r_{1/2}$ as function of absolute magnitude M_V. The colored ellipses represent the typical locations of elliptical galaxies and bulges (bright red), spiral galaxies (blue), galactic nuclei (purple), and late-type plus spheroidals (dashed gray). Local Group dwarf galaxies are plotted as open pentagons, blue for systems with gas and yellow for systems without. The uFds are represented as star symbols and use the same colour code.

Stellar feedback would accelerate metal-rich gas beyond the escape velocity of the shallow potential wells of dwarf galaxies, which then halts star formation and stops further chemical enrichment. A mechanism like this could regulate both the chemical evolution

and the growth of the galaxy, and would help explain the continuity of structural properties we observe from dwarfs to larger systems.

Detailed numerical models that are successful in reproducing the observed properties of dwarfs galaxies seem to corroborate the idea that their chemical enrichment is dominated by gas and metal loss (Matteucci and Tosi, 1985; Marconi et al., 1994; Carigi et al., 1995; Salvadori et al., 2008). But we note how there is still controversy on the theoretical side about whether stellar activity alone is effective at regulating dwarf galaxy structure, or if AGN feedback is also a necessary ingredient to explain the observed properties (Keller et al., 2016; Silk, 2017; Dashyan et al., 2017; Barai and de Gouveia Dal Pino, 2018; Koudmani et al., 2019).

1.1.1 The cosmological perspective

Nowadays our understanding of galaxy formation is based on the idea of hierarchical structure formation, a generic feature of Cold Dark Matter (CDM) models. In a ΛCDM universe, after the dark matter decouples from the baryons and radiation it collapses into halos, serving as the sites where these same baryons would later aggregate to form stars and galaxies (Gawiser, 2005).

Because the smallest structures collapsed first, dwarf galaxies were the first galaxies to form, and so they are the likely hosts of the first stars and BHs, as we will elaborate in the following sections. Their widespread distribution means dwarf galaxies could contribute significantly to the reionization of the Universe at $z \sim 8-10$ (Stark et al., 2007; Choudhury et al., 2008). Then as time marches on, nearby dwarfs come together and merge to create larger systems, while those initially more isolated are left unperturbed and may serve as relics from this early phase of galaxy assembly. From this perspective we are tempted to look at dwarf galaxies as local analogues for the first galaxies, offering us a unique window to study galaxy evolution in miniature.

Nevertheless, some sources of tension between theory and observations have risen in the last decades following the developments of large scale cosmological simulations. For instance, it has been noted that these simulations tend to overestimate the abundance of dark matter sub-halos and luminous ($L_{\rm tot} \gtrsim 10^5 L_\odot$) satellites of galaxies in the local group in what became known as the "missing satellites"problem (Klypin et al., 1999; Moore et al., 1999; Kravtsov, 2010). Another discrepancy is the cusp/core problem, in which we

see an approximately uniform dark matter density profile in the inner regions of dwarf galaxies, right where the simulations say we should see a power-law behaviour (de Blok, 2010; Boylan-Kolchin et al., 2011).

Some authors try to resolve these tensions by proposing changes to the assumptions underlying the standard ΛCDM cosmology (Zavala, 2009; Elbert et al., 2015; Bose et al., 2016; Schneider et al., 2017), while others explore if the effects of feedback from IMBHs are to blame (Barai and de Gouveia Dal Pino, 2019; Lanfranchi et al., 2021). We already have observational evidence for at least a few dwarf galaxies displaying AGN-driven outflows which exceed the escape velocity of their hosts (Manzano-King and Canalizo, 2020; Liu et al., 2020). It therefore seems reasonable that these outflows could rival or even supersede SN winds as the dominant gas loss mechanism in low-mass galaxies, alleviating some of the tensions outlined above as was pointed out in Silk (2017).

This was not at all an exhaustive list of all the ways studying dwarf galaxies can improve our understanding of galaxy formation. But it hopefully illustrates the kinds of opportunities dwarfs offer us to test our theories of structure formation and evolution in the Universe; and of particular interest to us in the following sections, the activity of the IMBHs they may harbor.

1.1.2 Evidence for IMBHs in dwarf galaxies

The first observational evidence for IMBHs in dwarf galaxies came in the late 80's when high-ionization narrow emission lines were found in the spectrum of the dE galaxy Pox 52 and of the spiral NGC 4395 (Kunth et al., 1987; Filippenko and Sargent, 1989).

Unfortunately, the most reliable way to measure the mass depends on us being able to resolve the gas or stellar dynamics inside the region where the BH's gravitational effects dominate over that of the galaxy, the so-called BH sphere of influence (see Equation 1.1). This means we are left to rely on electromagnetic signatures of accretion for objects further than a few Mpc (Nguyen et al., 2018). This is done by relying on the assumption of virialization to interpret the detection of a persistent broad Hα line component in the spectrum (Greene and Ho, 2005; Thornton et al., 2008), or by measuring the time-lag between continuum and emission-line variability through reverberation mapping (Peterson, 2005). These methods were applied to Pox 52 and NGC 4395 to find BH masses on the

order of $\sim 3\times10^5 M_\odot$. In the absence of a good mass estimate that can distinguish between them some authors just refer to both IMBHs and SMBHs as massive black holes (MBHs) to separate them from their stellar-mass counterparts.

$$r_{\rm i} = \frac{GM_{\rm BH}}{\sigma^2} \sim 0.1 \left(\frac{M_{\rm BH}}{10^5\ M_\odot}\right) \left(\frac{\sigma}{70\ {\rm km/s}}\right)^{-2}\ {\rm pc} \tag{1.1}$$

$$r_{1/2}^{\rm min}/r_{\rm i} = 300\ , \quad \text{where } r_{1/2}^{\rm min} = 30 \text{ pc, from Figure 1.1.} \tag{1.2}$$

Other IMBH candidates were found in works that searched through the SDSS data for accretion signatures like Greene and Ho (2004, 2007) and Dong et al. (2012), but these were spurious cases inside samples of mostly massive ($> 10^{10} M_\odot$) galaxies. The first systematic search for active MBHs exclusively in dwarf galaxies was performed in Reines et al. (2013), and their selection resulted in a sample of 136 dwarfs displaying narrow-line ratios indicative of photo-excitation by the hard radiation field of an AGN. 10 of these had their masses estimated to be $\sim 10^5 - 10^6 M_\odot$ following the virial method (see Section 2.1), and a follow up of them using Chandra X-ray data was done in Baldassare et al. (2017), yielding the detection of bright ($L_{0.5\text{-}7{\rm keV}} \simeq 10^{39} - 10^{42}$ erg/s) nuclear X-ray emission in all of them, with inferred Eddington fractions of the order of $0.1\% - 50\%$. However, as we will discuss in the Section 2.1, optical diagnostics can miss obscured and radiatively inefficient AGN (Ho, 2005; Narayan, 2005), as well as those located in more metal-poor dwarf galaxies with moderate levels of SF.

Later works improved this picture by looking for other AGN signatures in dwarfs. For example, a cross-match between the SDSS and 3XMM DR7 catalogue is done in Birchall et al. (2020) to find a sample of 61 dwarfs with X-ray luminosities above the expectation from X-ray binaries and from the hot diffuse gas. Following their criteria, the detection rate of dwarf AGN with $L_X \geq 10^{39}$ erg/s was found to be $\lesssim 6\%$ for galaxies with $M_* \lesssim 3\times10^9$. Notably, even though the X-ray luminosity of these objects is comparable with that of the objects from Baldassare et al. (2017), most of them are placed in the SF region of the BPT diagram. In Reines et al. (2020) the authors use the Very Large Array (VLA) Faint Images of the Radio Sky at Twenty-cm (FIRST) survey and find at least 13 dwarf galaxies with strong and compact radio sources too bright at 9 GHz to be explained as thermal HII regions or a from populations of supernova remnants (SNRs).

Even more recently, coronal lines are getting some attention as their potential to reveal hidden MBHs is starting to be explored. Coronal lines are forbidden emission lines with high-ionization potentials (> 90 eV) that are not typically produced by stars, and thus are considered reliable AGN indicators (Penston et al., 1984; Prieto and Viegas, 2000). The recent works of Kimbro et al. (2021) and Molina et al. (2021) have identified the [Fe X]λ6374 coronal line (with an ionization potential of 262.1 eV, Oetken, 1977) together with strong VLA radio detections in two different dwarf galaxies, which they interpret as evidence for the coronal lines being excited mechanically by jet-driven shocks. Based on this finding, a search for dwarf galaxies exhibiting the [Fe X]λ6374 line was performed in Molina et al. (2021), resulting in a sample of 81 coronal line AGN candidates with line intensities above $10\times$ the peak brightness of the line in the supernova event SN2005ip (Smith, 2009). Some of these candidates also had radio and X-ray detections.

We hopefully made clear how recent the investigation of the MBHs of dwarf galaxies is, with a diverse range of search methods resulting in a list of candidates that is growing everyday. Common to all of these different methods is the possibility of contamination from non-AGN objects, and in Chapter 2 we will see examples of the sort of caution one needs to take in order to not let star formation or X-ray binaries contaminate you sample of candidate dwarf AGN. For now, we note how the high-energy (HE, i.e. > 100 MeV) properties of these objects remains unexplored.

1.2 The seeds of SMBHs

Thanks to the efforts of astronomers trying to understand other island universes in the XX century, we now know that supermassive black holes (SMBHs) with $M_{\rm BH} \gtrsim 10^6 M_\odot$ inhabit the center of all massive galaxies. In order to recognize the relevance of the little monsters we want to investigate, it will be valuable to dedicate a few lines reviewing how our current understanding of the largest beasts in our Universe was developed.

The first hints that some galaxies contain powerful sources of electromagnetic radiation in their cores in addition to stars came in 1943 when Carl Seyfert identified high-excitation emission lines in the spectra of six spiral galaxies (Seyfert, 1943). This source remained a mystery for more than two decades, until it was realized that the accretion of interstellar matter onto a SMBH could supply the vast amounts of energy necessary to illuminate the

brightest seyfert galaxies, while the relative compactness of the BH explained the variability timescale of active galactic nuclei (AGN) (Salpeter, 1964; Zel'dovich and Novikov, 1964; Lynden-Bell, 1969).

Around the same time, people studying the spectra of quasars were finding peculiar broad emission lines at unfamiliar wavelengths (Oke and Schmidt, 1963; Greenstein and Matthews, 1963; Schmidt and Matthews, 1964). It was Maarten Schmidt who noticed, by investigating the spectra of 3C 273 in 1963, how those unfamiliar lines could be accounted for by the Balmer series of the hydrogen atom, assuming it was somehow red-shifted by $z = \frac{\lambda_{\text{obs}}}{\lambda_{\text{emit}}} - 1 = 0.16$ (Schmidt, 1963). The two main interpretations which arose to explain this depended on either gravitational or cosmological effects (see Greenstein and Matthews, 1963). According to the first, the gravitational field around the radiating source was so strong that the emitted photons lost a significant fraction of their energies climbing out of the quasar's potential well before escaping to infinity; this is a general relativistic effect that had been used previously by Walter Adams in 1925 to successfully explain the red-shifted Hα line from the Sirius B white dwarf (Holberg, 2010). The second interpretation postulated that quasars were far enough away from us that the very expansion of the Universe had to be taken into account, as photons naturally lose energy when traveling cosmological distances inside an expanding space.

Decisive evidence for the cosmological interpretation was provided in 1971 by the work of James E. Gunn, who showed that two galaxies containing quasars had the same redshifts as the quasars themselves (Gunn, 1971). Such interpretation could also make sense of the sequence of absorption features seen in the spectra of more distant quasars (Lynds, 1971), as these could arise from the clouds of neutral hydrogen present in the intergalactic medium between us and the quasar absorbing the portion of higher-energy photons which were red-shifted to wavelengths close to that of Lyα (1215.67 Å); a phenomena known as the Lyman-alpha forest (Weinberg, 2003).

By the late 60's quasars out to $z = 2$ were already known, and the techniques developed in the subsequent decades by the likes of Smith, Osmer, Schmidt, Schneider, Gunn and Warren, have both increased the number of quasars detected as well as the redshift limit we could observe them at. The greater statistics allowed for population studies that revealed how these objects also evolve in cosmological timescales (Schmidt et al., 1995; Osmer, 2003;

Croom et al., 2004; Fan, 2006).

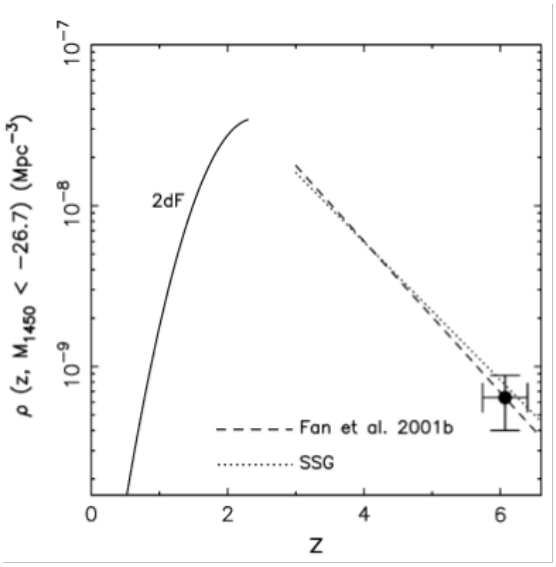

Figure 1.2: Plot from Fan (2006) showing the quasar comoving spatial density as function of redshift, limited by absolute magnitude at 1450 Å $M_{1450} < -26.7$ (or $L > 10^{46}$ erg/s). The dashed and dotted lines are the best-fit models from Fan (2001) and Schmidt et al. (1995) respectively. The solid line is the best-fit model from the quasar Two Degree Field (2dF) survey (Croom et al., 2004) at $z < 2.3$.

igure 1.2 shows the spatial comoving density of quasars as function of redshift as derived from combining observations from the 2dF QSO redshift survey with more recent observations of $z > 4$ objects. Interestingly, we see an increasing number of quasars up to $z \simeq 2$ and then a steep decline for larger values of z. The recent drop-off in the quasar comoving density for $z < 2$ is likely attributable to a decrease in activity, rather than the naive interpretation of the local Universe having a fewer number of SMBHs when compared with its more distant past. Therefore, as long as SMBHs do not evaporate on timescales anywhere near the Hubble time, we should expect most of today's galaxies to contain "dead"quasars (Soltan, 1982); and indeed about 40% of nearby galaxies host LLAGN with accretion rates less than 1% the Eddington rate (Ho et al., 1997; Ho, 2003).

Changing our focus now to the high-redshift end of Figure 1.2, if we adopt a standard ΛCDM cosmology along with fiducial parameters $H_0 = 73$ km s^{-1} Mpc^{-1}, $\Omega_m = 0.3$, $\Omega_\lambda = 0.7$ or similar, there is no escaping the implication set by the mere existence of quasars at $z \gtrsim 6$, namely that these SMBHs already had millions to billions of solar masses when the universe was less than a billion years old!

This fact challenges our understanding of how these objects can form and grow over

cosmic time. Did they start off with stellar masses ($\sim 10 M_\odot$) like today's BHs and then went through an intense period of nearly continuous super-Eddington accretion, or did some unknown mechanism that only operated in the early Universe produced "seed"BHs in the intermediate mass range that could then more easily grow to supermassive status?

Nowadays we have examples of quasars out to $z \sim 7$ (Mortlock, 2011; Bañados, 2017), which naturally raises the question of how SMBHs could have formed so quickly after the Big Bang. The 3 main proposed channels of seed BH formation and their possible different observational implications are summarized by Figure 1.3, where we see how the direct collapse channel would produce fewer and more massive seeds (up to $\sim 10^5 M_\odot$) in comparison to the Population III channel ($\sim 10^2 M_\odot$) for instance. For more details we recommend the excellent reviews of Haiman (2013) and Greene et al. (2020).

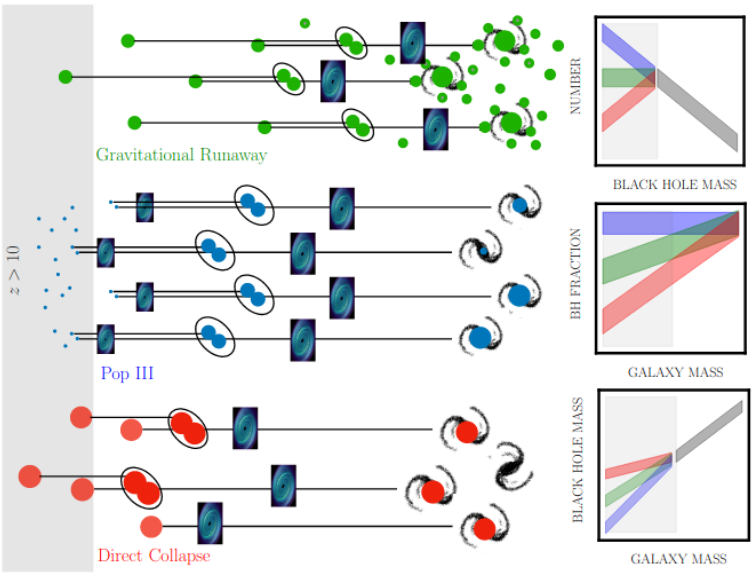

Figure 1.3: Possible observable differences between different seeding scenarios from Greene et al. (2020). Seed formation by Population III stars (blue) and direct collapse (red) channels occur at $z > 10$, while gravitation runaway (green) could happen throughout cosmic time. Mergers between seeds (black ovals) emit gravitational waves, and accretion episodes (blue disks) can be observed as AGN. The squares on the right show how black hole mass functions, occupation fractions, and black hole-galaxy scaling relations in the local Universe may differ depending on the seeding channel.

It is important to note how, after the formation of the seed BH, accretion and mergers will affect the final mass in all scenarios, but since dwarf galaxies are relatively isolated, it could be the case that their BHs have accreted less and merged less often than the SMBHs of their larger cousins, leaving them more similar to their progenitor seeds than to the

engines of luminous quasars (Greene, 2012; Mezcua, 2019; Reines, 2022). If so, there is hope that studies of MBH demographics in local dwarfs could help us constrain the seeding mechanism (Volonteri et al., 2008; Bellovary and Volonteri, 2011).

1.3 γ-rays from BHs

In this work, we intend to investigate whether dwarf AGN are γ-ray emitters. γ-rays carry information about the relativistic particle population responsible for their emission, and so they may help us identify the HE physics operating in these extreme environments (Dermer and Giebels, 2016).

For example, BHs at all scales often display radio jets. These are collimated structures composed of particles that were somehow accelerated to relativistic speeds by the intense magnetic field close to the BH. The jet's energetic electrons can produce γ-rays by inverse-Compton scattering low-energy photons coming from external radiation fields, or from the synchrotron photons they themselves emit while spiraling around the jet's magnetic field as in the synchrotron self-Compton (SSC) scenario (Finke et al., 2008; Takami, 2011; Nemmen et al., 2011; Böttcher et al., 2013). Moreover, the most powerful jets shock the ISM as they travel and can inflate huge cavities that we observe as surface brightness depressions in the X-ray emitting gas of some galaxies (Biller et al., 2004; Cavagnolo et al., 2010).

The most popular mechanism describing the launching of BH jets is the one proposed by Robert Blandford and Roman Znajek (BZ, Blandford and Znajek, 1977). According to it, the frame-dragging effect of the ergosphere causes magnetic field lines to tangle around the event horizon. The field lines then expand due to magnetic pressure and drag the plasma along with them, transferring the rotational energy of the BH to the outgoing matter which is ejected in form of two collimated relativistic jets. A order of magnitude estimate for the total power carried by the jet can be obtained using the expression from Tchekhovskoy et al. (2010) (Equation 1.3); it involves the magnetic flux threading one hemisphere of the BH Φ, the angular velocity of the event horizon Ω_H, the magnetic field at the horizon in Gauss B, and the dimensionless spin parameter a.

$$P_{BZ} \simeq \frac{\Phi^2 \Omega_H^2}{20\pi c} \sim 10^{41} \left(\frac{M_{\rm BH}}{10^5\ M_\odot}\right)^2 \left(\frac{B}{10^5 {\rm G}}\right)^2 a^2 \quad {\rm erg/s} \tag{1.3}$$

If the BZ mechanism captures the essentials of jet physics, we should expect the jet of

a maximally-rotating ($a \sim 1$) IMBH with $M_{\rm BH} \sim 10^5 M_\odot$ to reach powers in the range of $10^{37} - 10^{41}$ erg/s (for $B \sim 10^3 - 10^5$ G). A significant fraction of this energy could then end up converted into detectable γ-rays (Nemmen et al., 2012).

Another possible source of HE photons in AGN is the accretion flow itself. In contrast to the standard thin disk idea (Shakura and Sunyaev, 1973), in radiatively inefficient accretion flows (or RIAFs Ichimaru, 1977; Narayan and Yi, 1994; Narayan and McClintock, 2008) the plasma retains most of its gravitational energy as heat instead of radiating it away, which means the ions can reach temperatures up to $T_i \sim 10^{12}$ K close to the event horizon; essentially the virial temperature (see Equation 1.5). These conditions allow the production of neutral pions π^0 through proton−proton interactions, which then quickly decay into pairs of GeV photons (Mahadevan et al., 1997; Oka and Manmoto, 2003).

$$2K = -U \quad \Longleftrightarrow \quad 3k_b T = \frac{3GMm_p}{5R} \tag{1.4}$$

$$\therefore \quad T = \frac{GMm_p}{5k_b R} = \frac{m_p c^2}{10k_b}\left(\frac{R_S}{R}\right) \simeq 10^{12}\left(\frac{R_S}{R}\right) \text{K} \tag{1.5}$$

The transition from a thin disk to a radiatively inefficient flow is thought to take place when the accretion rate falls bellow a few percent of the Eddington rate ($\dot{m} = \dot{M}/\dot{M}_{Ed} \lesssim 0.01$). This RIAF model is successful in explaining both the "hard"spectral state of XRBs and the weak activity of low-luminosity AGN (LLAGN, Ho, 2009; Yuan and Narayan, 2014; Nemmen et al., 2014).

Additionally, AGN outflows in general, be it in the form of jets or spherical winds, induce shocks in the host galaxy's ISM that can lead to the stochastic acceleration of particles and the emission of γ-rays (Wang and Loeb, 2016; Lamastra, 2017; Ajello, 2021). X-ray observations of nearby AGN have identified blue-shifted Fe K-shell absorption lines that are believed to be caused by outflowing material in the form of fast spherical winds, the most powerful of which can reach speeds up to $\sim 0.3c$ (Reeves et al., 2003; Tombesi et al., 2010; Gofford and Reeves, 2013). The mechanical power of these fast winds is $\gtrsim 10^{41}$ erg/s, high enough to significantly impact the host's gas an maybe even unbind it from the galaxy's potential altogether (Cicone, 2014; King and Pounds, 2015). Theoretical modeling even suggests the cosmic rays (CR) accelerated by AGN winds could account for a significant fraction of the neutrino background (Wang and Loeb, 2016, 2017; Liu et al., 2018).

1.4 The *Fermi*-LAT

Launched in 2008, the *Fermi Large Area Telescope* is a pair-conversion telescope which relies on detectors similar to those found in particle accelerators. It has greater effective area, wider field of view and energy interval, and higher spatial and temporal resolutions than its predecessor, the *Compton Gamma Ray Observatory* (CGRO).

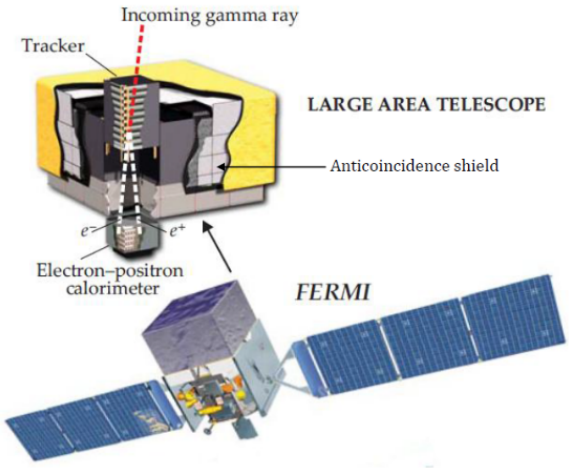

Figure 1.4: The *Fermi*-LAT and its main components. Figure adapted from Thompson et al. (2012).

The LAT tracker consists of a 4×4 matrix of multiple stacked layers of alternating silicon plates and tungsten foil where incoming γ-rays interact to start electron-positron cascades. This is illustrated in the scheme of Figure 1.4. The silicon layers track the trajectory of the charged particles and the calorimeter measures their final energy, allowing us to reconstruct the energy and direction of the primary γ-ray. The LAT is sensitive to photons with energies in the 20 MeV $-$ 500 GeV band, achieving its best performance around 1 GeV (see Atwood, 2009, for more details).

The *Fermi*-LAT scans the whole sky in about 3 hours and has been doing so since launch, accumulating hundreds of GBs of science-rich data and massively contributing to our understanding of the γ-ray sky in the process (Massaro et al., 2015). Thus, it is a great tool to employ in our search for the emission of what are likely to be faint sources of HE photons.

1.5 Motivation and goals

Having established some of the open questions regarding the presence and role of MBHs in dwarf galaxies, we now focus on the specific goal of the present work. As stated previously, the main question we wish to address is whether active MBHs in dwarf galaxies are γ-ray emitters, and if possible, also answer how such emission might come about. To this end we have used over 13 years of *Fermi*-LAT observations to analyse a sample of 135 dwarf galaxies containing AGN signatures in different regions of the electromagnetic spectrum.

Since we expect these little monsters to be weak γ-ray emitters ($L \sim 10^{39} - 10^{42}$ erg/s, judging by their luminosity in other bands) we employ a stacking technique inspired by the ones done in Paliya et al. (2019) and de Menezes et al. (2021) to study the cumulative signal of sources that are likely too faint to be detected individually. Stacking analyses of *Fermi* data have previously been used to probe the collective emission from weak populations such as extreme blazars ($\nu_{\rm syn}^{\rm peak} \geq 10^{17}$ Hz, Paliya et al., 2019) and star-forming galaxies (Ajello et al., 2020). It therefore constitutes a great tool for us to utilize in our search.

Chapter 2

Observations

We start this chapter by going into more detail about previous works that have searched for AGN in dwarf galaxies by using different signs of MBH activity and use them as a base to build our own sample of dwarf AGN. Then, we briefly go over the basics of maximum likelihood analysis as applied for *Fermi* data, and move on to explain the stacking method implemented in our search for the collective γ-ray signal from targets that have proven too faint to be detected individually.

On the interest of building a sample of dwarf galaxy AGN to stack in γ-rays, we search the literature for recent works that have looked for signatures of MBH activity in nearby dwarfs. As we will explain in the proceeding discussion, our final AGN sample consists of 135 candidates, which can be separated into 4 sub-samples based on the MBH signatures used to detect them: Optical narrow-lines from Reines et al. (2013) and Manzano-King and Canalizo (2020), Radio emission from Reines et al. (2020), X-rays from Birchall et al. (2020), and the [Fe X] coronal line from Molina et al. (2021). We arbitrarily select objects from the works discussed above, prioritizing those for which we have SDSS-derived information in the NASA-Sloan Atlas[1] (NSA), like basic host galaxy properties and emission-line fluxes (York, 2000; Aihara, 2011).

2.1 Optical narrow-lines

AGNs and H II regions have been noticed to separate cleanly in the two-dimensional diagram involving the ratios of narrow emission lines [O III]λ5007/Hβ and [N II]λ6583/Hα, also known as the Baldwin, Phillips and Terlevich (BPT, Baldwin et al., 1981; Veilleux

[1] http://nsatlas.org/

and Osterbrock, 1987) diagram. This is believed to be due to the much harder radiation field of AGN being able to photoionize the host galaxy's ISM to a higher degree when compared to stars, and so the BPT diagram is used routinely to find AGN-like excitation in galaxies.

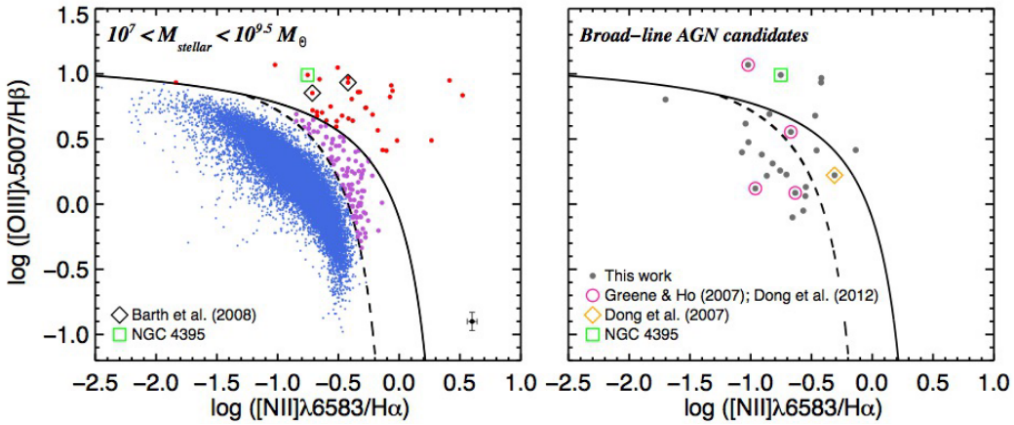

Figure 2.1: Left: BPT diagnostic diagram of all dwarf galaxies analysed in Re13. AGN, SF, and composite objects are displayed as red, blue, and pink dots respectively. The solid and dashed lines correspond to the empirical separations of Kewley 2006 and Kauffmann 2003b. Right: BPT with the broad-line objects only.

In Reines et al. (2013) (hereby Re13) the authors present a sample consisting of 136 dwarf galaxies ($M_* \lesssim 10^{9.5} M_\odot$) selected from the NSA that are classified as either AGN or composite objects by the BPT diagram. These are shown in Figure 2.1 along with the $\sim$ 25000 other dwarfs from their parent sample.

10 of the BPT AGN also displayed an additional broad Hα component in their spectra with FWHM $>$ 500 km/s, which was used to estimate the BH mass following the approach outlined in Greene and Ho (2005) and summarized by Equation 2.1. The broad Hα is assumed to be emitted by virialized gas orbiting the BH at large speeds, i.e., $M_{\rm BH} \propto RV^2/G$, where for the velocity of the gas V they use the full width at half-maximum of the Hα line while for R they take the radius of the BLR as estimated by a modification of the $R_{\rm BLR} - L_{5100}$ relation from Bentz (2013) (Equation 2.2) in which the luminosity of the broad Hα line is used as a proxy for the continuum luminosity at 5100 Å (Equation 2.3). The values obtained by this approach lie on the range of $10^5 - 10^6 M_\odot$.

$$M_{\rm BH} = \epsilon \left(\frac{R_{\rm BLR} {\rm FWHM}^2_{\rm H\alpha}}{G} \right) \qquad , \text{with } \epsilon \simeq 1 \tag{2.1}$$

$$\log\left(\frac{R_{\rm BLR}}{\text{lt-days}}\right) = 1.555 + 0.542\log\left(\frac{L_{5100}}{10^{44}\ \text{erg/s}}\right) \tag{2.2}$$

$$L_{\rm H\alpha} = 5.25\times10^{42}\left(\frac{L_{5100}}{10^{44}\ \text{erg/s}}\right)^{1.157}\ \text{erg/s} \tag{2.3}$$

While the BPT diagram is generally a good tool for finding cases where the AGN dominates over star as the main source of excitation in massive galaxies, there is evidence of it being a less reliable diagnostic when applied to dwarf galaxies. In particular, the sensitivity of the [N II] line to metallicity makes it difficult to identify AGN in low-metallicity environments using this line (Groves et al., 2006; Ludwig et al., 2012), as the lower [N II]/Hα ratio places these objects more to the left on the BPT diagram, potentially misclassifying them as star-forming. This is also true for other diagnostics employing the [N II] line such as the WHAN diagram (Fernandes et al., 2011).

Another confounding factor is the expected lower luminosity of lower-mass BHs, which causes their contribution to the excitation of the host's ISM to be diluted or entirely hidden by even moderate levels of stellar activity (Cann et al., 2019; Richardson, 2022). In the end, these limitations work to bias optical narrow-line selections towards finding the most luminous (or most radiative efficient) AGN in more metal-rich galaxies, making the use of other diagnostics necessary in order to get a more complete sensus of the dwarf galaxies hosting MBHs. As we are more interested in the activity of these BHs rather than their demographics, we used the work of Re13 as a base to build our optically selected sub-sample.

From Re13, we select 43 galaxies that are classified as either AGN or as a composite object, i.e., whose photoionization likely has some contribution from the MBH. As a consequence of the overlap between some of the accretion signatures, we also add to sub-sample O objects from the following works that are classified as AGN on at least one of the optical diagnostics explored, this includes 9 galaxies from Molina et al. (2021), some of which have radio emission in addition to the [Fe X] coronal line, and 3 from Manzano-King and Canalizo (2020) displaying ionized outflows. In total, this sub-sample contains 55 optical narrow-line selected AGN.

2.2 X-rays

X-ray emission from AGN can come from the hot ($T \sim 10^8$ K) Comptonized environments of the corona (Liang and Nolan, 1984; Haardt and Maraschi, 1991) or jets (Harris et al., 1994; Merloni et al., 2003; Nemmen et al., 2011). However, searches for X-rays from MBHs need to proceed carefully since their emission may be confused with that of X-ray binaries (XRBs).

A cross-match between the MPA-JHU[2], another SDSS value-added catalogue, and the 3XMM-Newton DR7 catalogue was done in Birchall et al. (2020) (hereafter Bi20) to find a sample of 61 dwarfs with X-ray luminosities above the expectation of XRBs and of hot diffuse gas. The expected contribution to the $0.5 - 2$ keV emission from the diffuse gas is calculated using the relation found by Mineo et al. (2012) of Equation 2.4 involving the SFR, while the contribution of XRBs is estimated by the relation of Lehmer (2016) shown in Equation 2.5, which scales with both SFR and stellar mass. We have omitted the redshift factors since we are interested in mostly local ($z < 0.1$) dwarfs.:

$$L_{\rm Gas}[\text{erg s}^{-1}] = 8.3 \times 10^{38} \text{SFR } [M_\odot yr^{-1}] \tag{2.4}$$

$$L_{\rm XRBs}[\text{erg s}^{-1}] = 2.3 \times 10^{29} M_*[M_\odot] + 1.9 \times 10^{39} \text{SFR}[M_\odot yr^{-1}] \tag{2.5}$$

They then use the estimates obtained from these empirical relations and implement the criteria of Equation 2.6 to filter the selected galaxies for excess emission. This is illustrated by the left panel of Figure 2.2. A resulting sample of 61 dwarf galaxies with X-ray luminosities likely attributable to AGN is produced.

$$\frac{L_X^{\rm obs}}{L_{\rm XRBs} + L_{\rm Gas}} \gtrsim 3 \tag{2.6}$$

The BPT classification of these objects is shown on the right panel of Figure 2.2, where we see how most of the objects in this sample lie in the SF region of the diagram. The authors also estimate the relative contribution of the AGN to the optical luminosity of the galaxy using a model SED from Berk et al. (2001), and find that most have $L_{AGN}/L_{gal} \lesssim 0.25$ confirming the idea that optical/UV AGN emission is hidden by SF, causing the BPT diagram to misclassify them.

[2] see http://www.mpa-garching.mpg.de/SDSS/DR7/

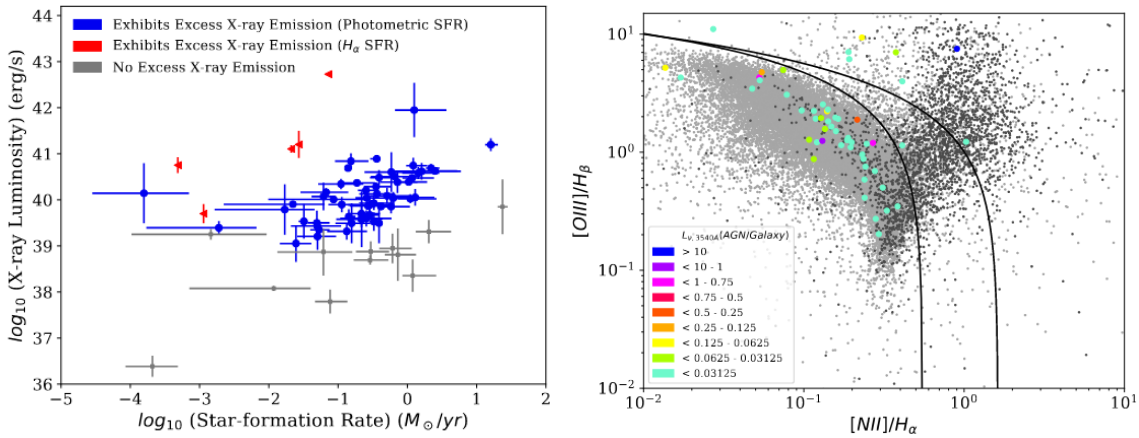

Figure 2.2: Left: X-ray luminosity as a function of star formation rate for the X-ray active dwarf galaxies from Bi20. Grey points correspond to galaxies that did not meet the X-ray excess criterion from 2.6. Right: BPT classification of the X-ray selected dwarf AGN. Colors represent different ratios of AGN and galaxy optical luminosity at 3450 Å, light grey are dwarf galaxies in the MPA-JHU, while dark grey are MPA-JHU objects with a X-ray counterpart, the latter are largely dominated by high mass AGN-like objects.

For sub-sample X we take 32 X-ray AGN candidates from Bi20, together with the 10 broad-line AGN from Re13 that were surveyed for X-rays in Baldassare et al. (2017). Additionally, Molina et al. (2021) used Chandra observations to find X-ray emission from 6 [Fe X]-selected dwarf AGN, two of which are also present in Re13. These 46 objects constitute our sub-sample X.

2.3 Radio

Radio emission is almost always seen in AGN, even weak LLAGN display extended radio emission when observed at high enough angular resolution (Ho, 2008; Mezcua and Prieto, 2014).

In Reines et al. (2020) (hereby Re20) the authors use the VLA Faint Images of the Radio Sky at Twenty-cm (FIRST) survey and find at least 13 dwarf galaxies with strong and compact radio sources too bright to be explained as coming from thermal HII regions. They do this by following Condon (1992) and determining the rate $Q_{\rm Lyc}$ of Lyman continuum photons (ionizing photons) that would be produced if the radio emission had a thermal origin:

$$Q_{\rm Lyc} \gtrsim 6.3 \times 10^{52} \left(\frac{T_e}{10^4 {\rm K}}\right)^{-0.45} \left(\frac{\nu}{\rm GHz}\right)^{0.1} \left(\frac{L_\nu^{\rm thermal}}{10^{20} {\rm W\ Hz^{-1}}}\right)\ {\rm s^{-1}} \tag{2.7}$$

and then using this value to estimate the predicted SFR following Kennicutt (1998):

$$\mathrm{SFR} = 1.08 \times 10^{-53} Q_{\mathrm{Lyc}} \; M_{\odot}\mathrm{yr}^{-1} \tag{2.8}$$

This SFR is then compared with another more direct estimate for the SFR based on the UV luminosity of the galaxy obtained from far-ultraviolet (FUV) flux measurements from the Galaxy Evolution Explorer (GALEX) and 22 μm (mid-IR) observations from the Wide-field Infrared Survey Explorer (WISE) from the AllWISE Source Catalog (see Section 4.4 for more details). Under the assumption that the radio emission is thermal, 19 of the objects would have implied SFRs larger than the SFR of their entire host galaxy, making it unlikely that thermal bremsstrahlung can fully account for the luminosity of these radio sources. This comparison is shown in Figure 2.3. They also discuss other possible origins for the radio emission like individual or populations of SNRs, but conclude that AGN is the most likely explanation.

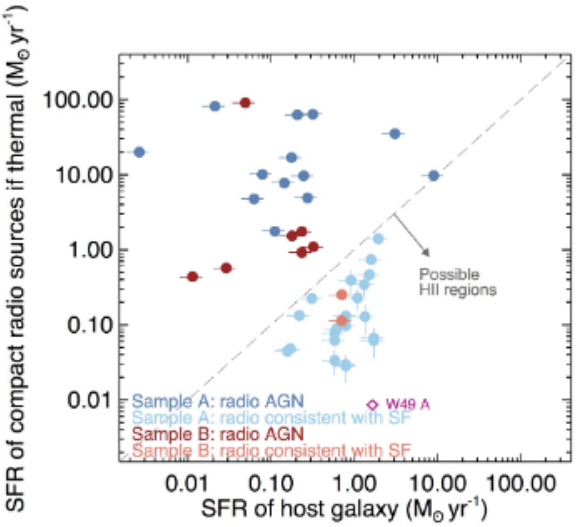

Figure 2.3: One of the plots from Re20 showing the comparison between the SFR obtained from the assumption of thermal radio emission and the SRF of the entire host galaxy. Sources above the one-to-one relation cannot be explained by this mechanism since individual HII regions cannot have SFRs exceeding the entire galaxy. Sources below the relation can be, but are not necessarily, HII regions. The Galactic massive star-forming region W49A is shown for comparison where the SFR of the MW is taken from Licquia and Newman (2015).

Notably, some of these objects have arcsecond offsets from their host galaxy's geometrical center, which the authors argue might hint at a gravitational potential too shallow to efficiently bring the BH to the nuclear region of the dwarf galaxy through dynamical friction (Governato et al., 1994; Bellovary et al., 2018; Ma and Hopkins, 2021).

We took all 19 radio AGN candidates from Re20 to build our sample R. This includes both the 13 best candidates and the other 6 that have poor redshifts with relatively large uncertainties, represented as red points on Figure 2.3. The same method outlined above was done in Molina et al. (2021) for the 5 galaxies displaying compact radio emission in addition to the [Fe X] coronal line, and a cross-match with the FIRST catalogue revealed radio detections in 4 of our X-ray selected AGN. Putting it all together results in a sub-sample of 28 radio-selected objects.

2.4 *[Fe X]λ6374 coronal line*

Coronal lines are highly-ionized emission lines originating from forbidden transitions with ionization potentials of at least 90 eV and critical densities on the order of $10^7 cm^{-3}$ Penston et al. (1984). The high ionization potential (I = 262.1 eV) of the [Fe X]λ6374 line makes it a reliable signature of BH activity, for it can be produced either through photoionization by a radiation field with enough photons with energies equal to the ionization energy or higher, or through collisional excitation at temperatures $\sim 10^6$ K (doing $3k_bT_e \sim I$).

From observations, both optical and near-infrared (NIR) coronal lines usually appear broader and blueshifted relative to lines of lower ionization stages (De Robertis and Osterbrock, 1984; Veilleux, 1991; Erkens et al., 1997) as is shown on the right panel of Figure 2.4. This has led to the idea that a coronal line region (CLR) exists somewhere in between the broad and the narrow-line regions, possibly close to the torus where the combined effect of shocks from outflowing material and the intense radiation field can produce the coronal lines (Rodriguez-Ardila et al., 2002; Müller-Sánchez and Prieto, 2011; Negus et al., 2021). However, the works of Kimbro et al. (2021) and Molina et al. (2021) identify the [Fe X] line together with strong VLA radio detections in two different dwarf galaxies, and they interpret their results as evidence for the coronal line being excited mechanically by jet-driven shocks.

Motivated by this idea, a search on the SDSS for dwarfs displaying this coronal line was realized in Molina et al. (2021) (hereafter Mo21) that resulted in a sample of 81 dwarfs with [Fe X] luminosities $> 10\times$ the peak brightness of the supernova event SN2005ip ($\sim 2\times10^{37}$ erg/s, Smith, 2009), which they argue is unlikely to be produced by ordinary stars.

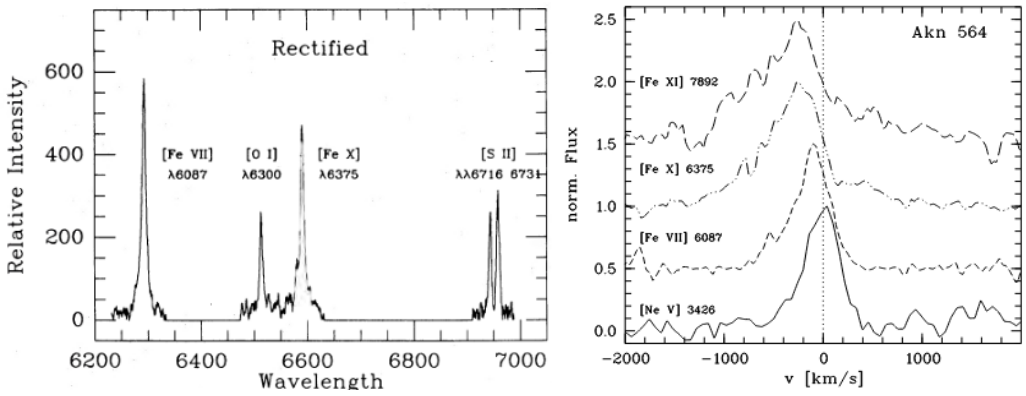

Figure 2.4: Left: spectral scan of III Zw 77 displaying the [Fe VII] and [Fe X] coronal lines from De Robertis and Osterbrock (1984). Right: Comparisson between observed profiles of different lines of Akn 564 from Erkens et al. (1997) showing the asymmetry and blueshifts of the higher-ionization iron lines.

46 of these [Fe X]-selected AGN constitute our sub-sample F. As stated previously, some of these objects are classified as AGN by the BPT and/or other optical narrow-line diagnostics while others show X-rays or radio emission, and so we add these to their respective sub-samples as well.

2.5 The sample of dwarf AGN

Putting everything together we end up with a final sample of 135 dwarf AGN to look for in γ-rays. These local dwarf AGN have redshifts and stellar masses in the $z \sim 0.01 - 0.14$ and $\log(M_*/M_\odot) \sim 7.3 - 9.7$ ranges, with means at $\bar{z} = 0.314$ and $\log(\bar{M}_*/M_\odot) = 9$. These objects can be separated into 4 sub-samples based on the accretion signatures used to detect them; 55 of them are optically-selected AGN, 46 have X-ray detections, 28 have radio detections, and another 46 display the [Fe X] coronal line.

It is important to note the overlap between these sub-samples as a result of a few objects displaying multiple signatures at the same time. We list all signatures exhibited by each target in column 5 of Table 2.1, denoting "O" for optical narrow lines, "X" for X-rays, "R" for radio and "F" for the [Fe X] line.

2.6 Control sample of SF galaxies

In addition to dwarf AGN, we also look for the γ-ray emission from 39 dwarf galaxies with similar properties to our AGN sample but which have no reported AGN signature,

and whose GeV emission would presumably come entirely from stellar processes.

We select 25 of the objects in this control sample from the NSA by applying the stellar-mass threshold ($M_* < 10^{9.5} M_\odot$) and redshift ($z \sim 0.01 - 0.14$) cuts. then we require they fall in the SF region of both [O III]/Hβ vs [N II]/Hα and [O III]/Hβ vs [O I]/Hα diagnostic diagrams, and checking the works cited in previous section to make sure they don't have any reported signs of MBH activity. The other 14 (SF26−SF39) are dwarf galaxies with radio properties consistent with SF activity listed in Re20. This control sample of non-AGN dwarf galaxies has a mean redshift of $\bar{z} = 0.0022$ and mean stellar-mass of $\log(\bar{M}_*/M_\odot) = 8.9$. Objects from this sample are also included on Table 2.1 with the "SF" flag.

Table 2.1 - List of target dwarf galaxies surveyed for γ-ray emission together with general host galaxy properties. Both AGN and SF targets are included. Column (1): ID designation of sources. Column (2): J2000 SDSS name. Column (3): Flag to denote the AGN signature or the sub-sample in which the target is included. Column (4)-(5): Equatorial coordinates of the dwarf galaxies in degrees. Columns (6)-(8): Galaxy properties from NSA v0.1.2 assuming $h = 0.73$, redshift z, log stellar mass in units of $M_\odot/h^2$, and log of SFR in $M_\odot yr^{-1}$ as derived from the relations of Kennicutt and Evans (2012).

ID	SDSS Name	Sub-sample	Ra	Dec	z	log(M_*)	log(SFR)
(1)	(2)	(3)	(4)	(5)	(6)	(7)	(8)
O1	J024656.39-003304.8	O, X	41.735014	-0.551378	0.0459	9.41	-0.848
O2	J090613.75+561015.5	O, X, R	136.55732	56.170986	0.0466	9.355	0.263
O3	J095418.15+471725.1	O, X	148.575645	47.29032	0.0327	9.121	-0.007
O4	J122342.82+581446.4	O, X, F	185.928463	58.246233	0.0144	9.465	-0.938
O5	J122548.86+333248.7	O	186.453617	33.546866	0.0011	9.102	-2.626
O6	J144012.70+024743.5	X	220.052935	2.795423	0.0299	9.458	0.464
O7	J085125.81+393541.7	O, X	132.857568	39.59494	0.041	9.407	-0.432
O8	J152637.36+065941.6	O, X	231.655695	6.994921	0.0384	9.328	-0.56
O9	J153425.58+040806.6	O, X	233.606639	4.135191	0.0395	9.116	-0.922
O10	J160531.84+174826.1	O, X	241.382722	17.807255	0.0317	9.24	-1.101
O11	J024825.26-002541.4	O	42.105274	-0.428173	0.0247	9.106	-1.598
O12	J032224.64+401119.8	O	50.602677	40.188822	0.0261	9.421	-0.657
O13	J081145.29+232825.7	O	122.938749	23.473824	0.0157	9.016	-1.629
O14	J082334.84+031315.6	O	125.895197	3.221042	0.0098	8.536	-0.68
O15	J084025.54+181858.9	O	130.106436	18.316401	0.015	9.275	-1.544
O16	J084204.92+403934.5	O	130.520539	40.659579	0.0293	9.301	-1.311
O17	J090222.76+141049.2	O	135.594862	14.180374	0.0297	9.413	-1.244
O18	J092129.98+213139.3	O	140.374956	21.527609	0.0313	9.306	-1.221

Tabela 2.1

ID (1)	SDSS Name (2)	Sub-samples (3)	Ra (4)	Dec (5)	z (6)	log(M_*) (7)	log(SFR) (8)
O19	J100935.66+265648.9	O	152.39862	26.946949	0.0144	8.435	-1.401
O20	J102252.21+464220.7	O	155.717595	46.705777	0.04	9.439	-1.213
O21	J110503.96+224123.4	O	166.266532	22.689843	0.0246	9.047	-1.539
O22	J110912.37+612347.0	O, X	167.301657	61.396408	0.0068	8.914	-1.287
O23	J111319.23+044425.1	O	168.330162	4.740341	0.0265	9.284	-1.326
O24	J114302.40+260818.9	O	175.760067	26.138609	0.023	9.259	-1.188
O25	J114359.58+244251.7	O	175.998313	24.714395	0.0501	9.475	-0.574
O26	J114418.83+334007.4	O	176.078519	33.668731	0.0325	9.383	-0.884
O27	J130434.92+075505.0	O	196.145514	7.918085	0.048	8.949	-1.077
O28	J130457.86+362622.2	O	196.241119	36.439538	0.0229	9.468	-1.584
O29	J133245.62+263449.3	O	203.190089	26.580376	0.047	9.393	0.373
O30	J134757.69+465434.9	O	206.990386	46.909691	0.0277	9.367	-1.204
O31	J134939.36+420241.4	O	207.41403	42.044824	0.0411	9.334	-0.784
O32	J140228.72+091856.4	O	210.619719	9.315675	0.0191	8.935	-1.529
O33	J140510.39+114616.9	O	211.293335	11.771371	0.0174	9.374	-1.509
O34	J141208.47+102953.8	O	213.035303	10.498284	0.0326	9.076	-1.005
O35	J142044.94+224236.8	O	215.187269	22.710264	0.0307	9.272	-1.322
O36	J143523.42+100704.2	O	218.847621	10.117833	0.0312	9.237	-0.66
O37	J144712.80+133939.2	O	221.803373	13.660914	0.0323	9.316	-1.146
O38	J153941.68+171421.8	O	234.923631	17.239383	0.0458	9.454	-0.73
O39	J154059.61+315507.3	O	235.248385	31.918697	0.0528	9.118	-0.148
O40	J100551.18+125740.6	O	151.463299	12.961306	0.0094	9.738	-0.312
O41	J010005.93-011058.8	O	15.024729	-1.183049	0.0514	9.34	-0.319
O42	J144252.78+205451.6	O	220.719942	20.91437	0.0427	9.083	-0.576
X1	J025645.82+060317.4	X	44.190968	6.054781	0.0262	9.509	-1.333
X2	J081432.21+515305.7	X	123.634299	51.884942	0.0392	9.45	-0.566
X3	J081938.80+210353.1	X	124.91171	21.064393	0.0141	9.325	-1.385
X4	J092720.43+362406.8	X	141.835258	36.401835	0.019	8.699	-1.717
X5	J102901.39+293809.0	X, R	157.255319	29.634876	0.0369	7.93	0.023
X6	J120746.11+430734.8	X, R	181.942145	43.126346	0.0032	9.593	-2.068
X7	J011523.96+003808.7	X	18.850109	0.63552	0.0352	8.259	-0.769
X8	J120900.89+422830.9	X	182.253722	42.475264	0.0236	9.534	-1.174
X9	J130708.43+535744.6	X, R	196.785168	53.962423	0.0294	9.245	-0.06
X10	J134427.29+560132.0	X, R	206.11397	56.025004	0.039	8.905	0.429
X11	J121831.72+055059.2	X	184.632182	5.849816	0.0076	8.476	-2.629
X12	J082228.93+034551.7	X	125.620593	3.764459	0.0351	8.96	-0.129
X13	J143102.57+281625.9	X	217.760801	28.273837	0.0318	9.014	-0.984
X14	J083200.50+191205.8	X	128.002137	19.201629	0.0375	9.39	-1.0
X15	J090335.40+151142.0	X	135.897482	15.195032	0.0288	9.012	-1.185
X16	J100805.11+125650.4	X	152.021332	12.947339	0.0317	9.533	-1.035
X17	J102526.59+124540.3	X	156.360874	12.761268	0.0309	9.036	-1.053
X18	J103410.14+580349.3	X	158.542359	58.06373	0.0075	7.354	-1.154
X19	J151412.19+134834.9	X	228.550776	13.809541	0.0223	8.865	-1.22

Tabela 2.1

ID	SDSS Name	Sub-samples	Ra	Dec	z	log(M_*)	log(SFR)
(1)	(2)	(3)	(4)	(5)	(6)	(7)	(8)
X20	J161321.25+510534.6	X	243.338732	51.092962	0.0336	9.474	-0.343
X21	J114013.23-002442.1	X	175.055134	-0.411706	0.022	8.903	-0.153
X22	J115558.40+232730.7	X	178.99342	23.458619	0.0521	9.33	-0.231
X23	J123520.20+393105.9	X	188.833486	39.519176	0.0209	8.179	-0.675
X24	J162729.76+385455.2	X	246.874055	38.915324	0.0324	9.012	-0.813
X25	J130033.66+273815.9	X	195.140316	27.637739	0.025	9.422	-0.146
X26	J134719.27+581437.5	X	206.830512	58.243779	0.0348	9.42	-0.477
X27	J142326.99+014326.0	X	215.863212	1.726245	0.0047	9.451	-1.633
X28	J144056.30+033140.9	X	220.235654	3.527517	0.0338	8.16	0.203
X29	J160651.01+080928.6	X	241.712578	8.157963	0.0093	8.176	-1.69
X30	J162642.49+390842.8	X	246.677034	39.145216	0.0283	8.789	-0.637
R1	J001900.30+150710.9	R	4.751339	15.119777	0.0368	8.645	-0.813
R2	J010607.17+004633.6	R	16.529894	0.776059	0.0174	9.404	-1.106
R3	J102740.99+011202.9	R	156.921447	1.201116	0.0218	7.823	-1.264
R4	J113648.57+125239.7	R	174.202429	12.877835	0.0345	9.317	-0.686
R5	J113642.72+264337.6	R	174.177971	26.727191	0.0333	9.243	-0.824
R6	J122603.63+081519.0	R	186.515172	8.255287	0.0246	9.312	-0.999
R7	J090313.10+482415.5	R	135.80456	48.404311	0.027	8.826	-1.237
R8	J090908.65+565522.1	R	137.28609	56.922894	0.0311	8.323	-0.824
R9	J093138.47+563319.0	R	142.910429	56.555272	0.0491	8.342	-0.689
R10	J120058.38-034116.3	R	180.243433	-3.688139	0.0264	9.235	-0.776
R11	J122011.25+302008.1	R	185.046924	30.335624	0.027	9.375	-0.796
R12	J125305.97-031258.7	R	193.274891	-3.216337	0.0227	8.603	0.756
R13	J235945.39+143504.0	R	359.938145	14.583897	0.0144	8.775	-1.174
R14	J162152.57+151855.9	X, R, F	245.469062	15.315555	0.0343	8.718	0.18
R15	J094918.02+165244.1	X, R, F	147.32514	16.878934	0.052	9.587	0.601
R16	J110508.30+444500.0	X, R, F	166.283808	44.746383	0.0215	9.265	0.495
R17	J004951.80-024243.0	R	12.466028	-2.711956	0.0133	9.009	-0.926
R18	J013408.69-074145.0	R	23.536425	-7.695966	0.0164	9.284	-1.503
R19	J024747.20+053519.9	R	41.947275	5.588036	0.0051	7.696	-2.318
R20	J085431.80-024058.9	R	133.632251	-2.683393	0.0153	8.619	-0.919
R21	J114318.69-032553.9	R	175.82777	-3.431248	0.0053	7.72	-2.049
F1	J135125.37+401247.7	O, X, F	207.855715	40.213241	0.0082	9.041	-0.887
F2	J094401.87-003832.1	X, R, F	146.007801	-0.642259	0.0048	7.748	-1.915
F3	J003218.60+150014.1	F	8.077542	15.003929	0.0179	8.23	-0.566
F4	J131603.91+292254.0	R, F	199.01634	29.381812	0.0378	8.93	0.471
F5	J153704.17+551550.8	X, F	234.267446	55.264129	0.0022	7.329	-2.832
F6	J092025.82+504939.7	F	140.107808	50.827789	0.0344	9.242	-0.854
F7	J165546.84+364047.5	O, F	253.945188	36.679872	0.0623	9.03	-0.689
F8	J131307.11+460554.3	O, F	198.279694	46.098379	0.0296	9.464	-1.189
F9	J124732.81+133705.2	O, F	191.886709	13.618171	0.0847	9.216	-0.552
F10	J091521.04+122615.1	F	138.83771	12.437524	0.0333	9.018	-0.505
F11	J135447.37+153004.2	F	208.697413	15.501164	0.024	9.461	-0.799

Tabela 2.1

ID (1)	SDSS Name (2)	Sub-samples (3)	Ra (4)	Dec (5)	z (6)	log(M_*) (7)	log(SFR) (8)
F12	J083908.64+331830.8	F	129.786051	33.308563	0.0544	9.148	-0.131
F13	J105544.62+462218.3	F	163.93592	46.371758	0.0507	8.891	-0.51
F14	J124430.39+404408.9	F	191.127239	40.736909	0.0179	9.238	-0.079
F15	J084527.60+530853.1	O, F	131.365003	53.148083	0.0311	8.462	0.077
F16	J210709.15-072522.3	F	316.788153	-7.422857	0.0283	8.716	-1.083
F17	J083025.53+330329.3	F	127.606431	33.058165	0.0209	9.161	-0.928
F18	J033553.12-003946.6	F	53.971329	-0.66295	0.0302	8.729	-1.084
F19	J011745.30-011032.1	O, F	19.438788	-1.175642	0.1088	8.86	-0.374
F20	J141623.30+330724.9	F	214.097114	33.123609	0.0832	9.4	0.196
F21	J133857.08+363545.0	F	204.737834	36.595857	0.0194	8.59	-1.094
F22	J133400.52+364200.1	O, F	203.502215	36.699999	0.0599	8.59	-0.718
F23	J104520.41+092349.0	O, F	161.33505	9.396973	0.0549	9.158	0.602
F24	J113449.15-010347.7	F	173.704846	-1.063236	0.0464	9.438	-0.654
F25	J150356.82-004200.2	O, F	225.98677	-0.70008	0.141	9.4	0.523
F26	J225236.35-003317.7	F	343.152075	-0.554778	0.0544	9.062	-0.176
F27	J085443.39+085652.6	F	133.680941	8.947908	0.0296	9.1	-0.712
F28	J111608.54+302232.9	F	169.035623	30.375825	0.0416	9.355	-0.82
F29	J142701.96+281534.2	F	216.758195	28.259495	0.0403	9.545	-0.744
F30	J110943.11+253800.1	F	167.429632	25.633357	0.0412	9.417	-0.814
F31	J082212.84+580142.2	F	125.55354	58.028416	0.0165	8.227	-1.479
F32	J142437.21+262039.0	F	216.154932	26.344126	0.0354	9.284	-1.327
F33	J141526.84+362429.7	F	213.861961	36.408279	0.0282	9.355	-1.23
F34	J003635.84-100303.6	F	9.14935	-10.051033	0.0208	9.471	-0.614
F35	J122058.35+562118.9	F	185.24318	56.355248	0.0346	9.51	-0.677
F36	J082449.86+383514.5	O, F	126.207924	38.587551	0.0304	9.097	-1.389
F37	J075204.18+424524.2	F	118.017493	42.756721	0.0411	9.296	-0.657
F38	J104200.36+122005.7	F	160.501536	12.334906	0.0026	8.082	-2.508
F39	J031618.15+010021.9	O, F	49.075654	1.006096	0.0331	8.793	-1.016
F40	J104919.28+375234.4	F	162.33046	37.876242	0.0253	9.223	-1.473
F41	J081329.70+544441.4	O, F	123.373709	54.744751	0.0323	8.991	-1.0
F42	J115117.60+671844.4	O, F	177.823292	67.312375	0.046	9.354	-0.505
SF1	J075912.03+341007.8	SF	119.800295	34.168786	0.0165	8.542	-1.424
SF2	J090905.48+472009.0	SF	137.272894	47.335881	0.0506	9.455	-0.775
SF3	J103148.28+542412.8	SF	157.951249	54.403588	0.0477	9.39	-0.69
SF4	J135012.82-022611.4	SF	207.553533	-2.436404	0.0238	9.217	-0.873
SF5	J143127.20-024009.5	SF	217.863425	-2.669554	0.0244	9.021	-1.04
SF6	J151652.29-015546.1	SF	229.217931	-1.929504	0.0339	9.268	-0.944
SF7	J083927.91+334250.9	SF	129.866318	33.714156	0.0538	9.2	-0.408
SF8	J094932.37+440801.9	SF	147.384989	44.133941	0.0151	8.587	-1.818
SF9	J111705.50+583100.6	SF	169.272799	58.516811	0.0053	8.368	-1.888
SF10	J115859.05+594211.6	SF	179.746002	59.703233	0.0424	9.464	-0.893
SF11	J124417.33+594307.9	SF	191.072248	59.718942	0.0098	8.269	-1.946
SF12	J132633.65+584050.6	SF	201.640207	58.680747	0.0233	8.607	-0.8

Tabela 2.1

ID	SDSS Name	Sub-samples	Ra	Dec	z	log(M_*)	log(SFR)
(1)	(2)	(3)	(4)	(5)	(6)	(7)	(8)
SF13	J112418.21+480847.4	SF	171.075891	48.146474	0.019	9.333	-1.005
SF14	J120722.50+485332.2	SF	181.843738	48.892212	0.0205	9.129	-1.371
SF15	J170003.90+324816.5	SF	255.016329	32.804603	0.0329	8.604	-0.852
SF16	J203848.84+000246.1	SF	309.703529	0.046133	0.0532	9.461	-0.571
SF17	J211928.96-002635.8	SF	319.870679	-0.443291	0.0506	9.375	-0.654
SF18	J092355.86+051105.9	SF	140.982768	5.184999	0.0277	9.2	-1.027
SF19	J100408.72+063037.7	SF	151.036339	6.510425	0.0042	8.106	-1.829
SF20	J104429.00+073029.2	SF	161.12084	7.508118	0.022	8.298	-0.742
SF21	J220142.68+000145.1	SF	330.427913	0.029153	0.0527	7.982	-0.684
SF22	J224244.49-003647.6	SF	340.685526	-0.613346	0.0525	8.971	-0.507
SF23	J140934.26+515646.2	SF	212.392889	51.946095	0.0065	7.576	-2.661
SF24	J145852.38+475416.3	SF	224.718061	47.904391	0.0303	9.234	-1.394
SF25	J155103.02+413318.1	SF	237.762645	41.554988	0.0231	8.654	-0.979
SF26	J011149.90-013917.9	SF	17.958251	-1.655107	0.0164	9.456	-0.455
SF27	J020525.99-075009.0	SF	31.358539	-7.835882	0.013	9.222	-0.366
SF28	J091643.69+594619.9	SF	139.18339	59.774721	0.0138	8.827	-0.358
SF29	J092601.20+192301.0	SF	141.504416	19.382872	0.0084	9.267	-0.903
SF30	J100248.69+431109.9	SF	150.704135	43.18821	0.0182	9.309	-0.378
SF31	J100351.86+592610.6	SF	150.966161	59.436268	0.01	9.448	-0.24
SF32	J103231.89+542403.5	SF	158.133231	54.400706	0.0048	8.934	-0.579
SF33	J104522.41+555737.5	SF	161.341828	55.961195	0.0031	8.577	-0.909
SF34	J110855.77+002641.3	SF	167.232409	0.4448	0.0129	9.027	-0.271
SF35	J112644.99+590924.9	SF	171.684538	59.15552	0.004	9.055	-0.802
SF36	J114536.93+311758.4	SF	176.403951	31.299553	0.006	9.425	-0.941
SF37	J115237.19-022809.9	SF	178.154968	-2.469432	0.0035	7.812	-2.101
SF38	J125314.55+042747.7	SF	193.310723	4.463235	0.0024	8.463	-1.937
SF39	J171853.44+301136.2	SF	259.722708	30.193403	0.0148	8.943	0.019

Chapter 3

Methods

The analysis of LAT observations is done by means of maximum likelihood estimation. What this means is that, for a given input model we compute its likelihood L, i.e., the probability of obtaining the data from the model, and then tweak the model's parameter in order to maximize L. The basic expectation is that a model with a greater likelihood will give a better description of the data at hand.

We won't go into detail of how exactly one computes the likelihood (see Cicerone[1]), but establishing these concepts here will be essential for the later chapters, where we will depend on the language of maximum likelihood analysis to talk about potential γ-ray sources with fluxes that may lie below LAT's sensitivity.

3.1 Comparing likelihoods

In any standard analysis of LAT data one needs to include in their model the distribution in the sky of all the relevant γ-ray sources that may contribute photons to the region-of-interest (ROI). This includes the known sources present in the 4FGL catalogues[2], as well as accounting for the diffuse (galactic) and isotropic (extragalactic) emissions[3]. Then you fit the model to the observations in order to get its maximum likelihood parameters and their uncertainties together with that model's corresponding likelihood.

By doing this and then comparing the likelihoods of different models one can find out which one is more likely, or which one better describes the data. When it comes

[1] https://fermi.gsfc.nasa.gov/ssc/data/analysis/documentation/Cicerone/Cicerone_Likelihood/

[2] https://fermi.gsfc.nasa.gov/ssc/data/access/lat/10yr_catalog/

[3] https://fermi.gsfc.nasa.gov/ssc/data/access/lat/BackgroundModels.html

to assessing the detection of individual sources, for instance, we compare the maximum likelihood values of a model containing that source L (the hypothesis) and of a model without it L_0 (the null-hypothesis); this comparison gets summarized by a quantity called Test Statistic $\mathrm{TS} = 2\ln(L/L_0)$. The square-root of the TS can then be used to quantify the significance of the hypothetical source ($\sqrt{\mathrm{TS}}$, see Mattox, 1996), where the gold standard criteria for a high confidence detection is $\mathrm{TS} > 25$ corresponding to a 5σ confidence level.

To get a sense of what this means say we have a model with likelihood L_0, we then add to it a new point source called 'PS' in a particular location and run the maximum likelihood estimation algorithm only to find $\mathrm{TS}_{\mathrm{PS}} = 25$, this means the ratio between the likelihoods L (model with PS) and L_0 (model without PS) is:

$$\frac{L}{L_0} = e^{\mathrm{TS}/2} \sim 2.7 \times 10^5 \tag{3.1}$$

or in other words, adding PS to that location made the model over 270 thousand times better at explaining the data than the previous one.

Inevitable uncertainties bring inevitable complications to this simple picture, but it hopefully does its job in illustrating why 5σ is the default standard a particular model has to meet before we declare it a new discovery; like the detection new particles (ATLAS Collaboration., 2012) or of new gravitational wave events (LIGO Collaboration, 2016). In essence, it represents the requirement that the hypothesis has to be much more likely than its alternative.

Our search for the γ-rays attributable to our target dwarf AGN includes photons in the $1 - 300$ GeV energy range that were intercepted by LAT between August 4, 2008 to September 17, 2021, covering over 13 years almost 300 GBs of data. The energy range was chosen because it is where the LAT has better angular resolution[4]. The binned likelihood analysis was carried out with `Fermitools 2.0.8`[5] and `fermipy v1.0.0`[6].

For each target we select all events detected in the front and back sections of the *Fermi*-LAT tracker (*evtype* = 3) that fall within a $10^\circ \times 10^\circ$ ROI centered on the target's coordinates. The modeling of each ROI is realized by using the standard configuration files and analysis parameters, like the latest model (as of mid-2021) of diffuse interstellar emission *gll_iem_v07*, the isotropic template *iso_P8R3_SOURCE_V2_v1*, all known sources

[4] `https://www.slac.stanford.edu/exp/glast/groups/canda/lat_Performance.htm`

[5] `https://fermi.gsfc.nasa.gov/ssc/data/analysis/software/`

[6] `https://fermipy.readthedocs.io/en/latest/`

from the 4FGL-DR2 catalogue within a 15° × 15° region around each target, as well as new point sources found with the `find_sources()` function from fermipy that exceeded the TS = 16 threshold (these are denoted with a "PS"in the name). In Figure 3.1 we show examples of a counts map and of the model used to describe it.

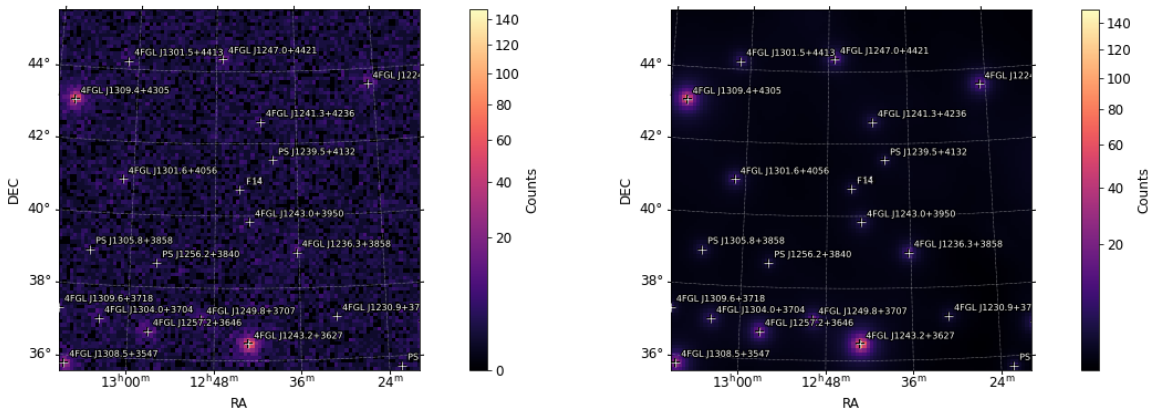

Figure 3.1: Left: example of a γ-ray counts map from the ROI centered around target F14. Right: the model used to fit the same region.

In order to maximize the likelihood of this model we perform at least two rounds of fitting using the MINUIT optimizer. The first is more encompassing, fitting all sources in the ROI simultaneously and setting their parameters close to their best fit values; the second one is more focused, so we only free the parameters of sources within 5° of the target while fixing the parameters of all others. We only accept the results when the reported Fit Quality is equal to 3, corresponding to a fully successful fit with an accurate covariance matrix[7].

We further study those targets showing TS > 9 (indicative of a $\gtrsim 3\sigma$ excess above the null) by reanalyzing them in the 500 MeV−300 GeV energy range and running `fermipy`'s `localize` and `lightcurve` functions. This inclusion of lower-energy photons is motivated by the hope that increasing the available statistics might lead to more robust results.

`localize`[8] is an iterative method that slightly varies the position of a point source in order to maximize its TS, but we only accept its output if the angular offset between the old and new positions are less than the estimated 99% positional uncertainty radius ($r99$). This is an iterative method that slightly varies the position of the point source of interest

[7] `https://fermipy.readthedocs.io/en/latest/fitting.html`

[8] `https://fermipy.readthedocs.io/en/latest/advanced/localization.html`

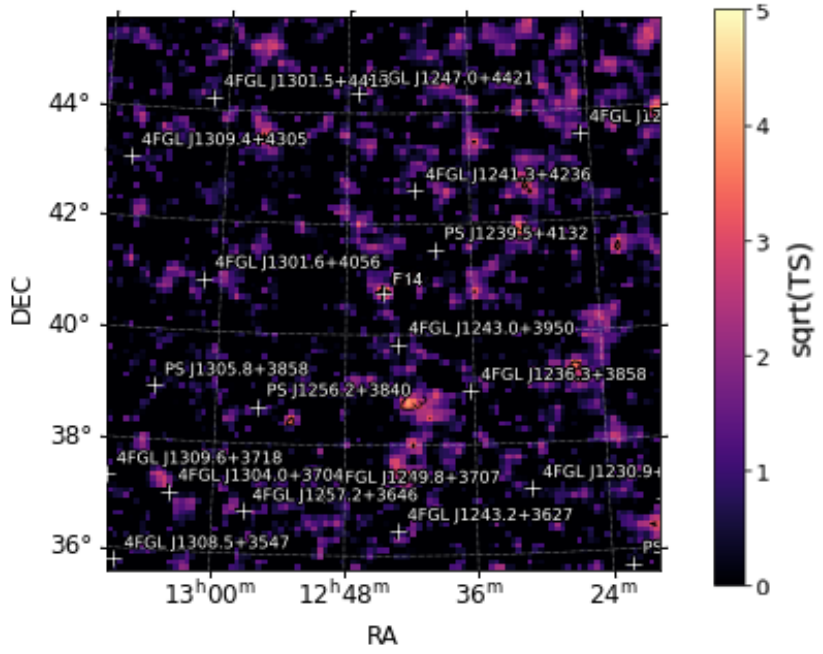

Figure 3.2: Left: Example of a spatial TS map for the ROI centered around target F14. The color scale represents value of $\sqrt{\text{TS}}$, or the significance a point source would have if it were added to the model in that particular spot in the ROI.

in order to maximize its TS. It does this by drawing a spatial TS map around the target, which is basically a map showing the likelihood of having a unmodeled point source at any given point of the ROI (see Figure 3.2 for an example). We only accept the output from `localize()` if the angular offset between the old and new positions are less than the calculated 99% positional uncertainty radius ($r99$) of the target. If this requirement is not fulfilled we return the target to its original position and add the nearby TS peak to the model as a new point source before re-doing the fit. By doing this we ensure that the new position is consistent with the direction of the original target within the estimated uncertainties, so we can be reasonably confident the observed signal is actually coming from the same direction of our dwarf galaxies instead of from a nearby TS peak not associated with them. A couple of targets have failed this requirement (X1, F6) and are shown in Figure 4.1.

We use the `lightcurve`[9] function to get the light curves of the most promising targets by dividing our $\sim$ 13 year dataset into 15 bins of $\sim$ 11 months. We then free all sources within 3° of the target and re-fit the model to the data in each bin; this gives us informa-

[9] `https://fermipy.readthedocs.io/en/latest/advanced/lightcurve.html`

tion about how the target's spectral properties and detectability changes with time. We save the details about the light curve analysis for Section 4.3.

3.2 The stacking procedure

As was hopefully made clear by the previous section, when working with potential sources at the threshold of detection we need to be careful not to overestimate the significance of our findings. Imagine we fit a model and get a TS just shy of 25 for a given target, should we consider it a real γ-ray source?

Notice in Figure 3.2 how blobs of moderate TS can arise in otherwise empty regions containing very few photons. What if a different model with the point source somewhere else entirely produces an ever greater overall likelihood? Worse still, it's possible that uncertainties in our modelling of diffuse emission can leave some photons unaccounted for in a particular spot of the ROI, which could be confused for a new point source. What if this happens close to our targets? How can we be sure we are looking at an actual faint source and not some residual fluctuation?

The answer is that we can't be sure, at least not when looking at faint targets individually. In order to probe the significance of a faint population composed of what we believe to be similar objects, we need a way to compare their combined likelihoods with that of spurious point sources. Here we outline our approach for stacking the likelihoods of our dwarf AGN and how we compare it with mock data to probe its true significance in a statistically meaningful way.

The first step for implementing a stacking analysis is to assume our targets have some property in common that we can stack over. Previous works employing γ-ray stacking have chosen for this task both the spectral shape, characterized by a simple power-law with index Γ, and the observed flux F_γ, where they trace 2D TS profiles along these two quantities (see Paliya et al., 2019; Ajello et al., 2020; Ajello, 2021). However, since we don't expect our targets to necessarily display similar fluxes we can instead just trace 1D TS profiles over the photon index space (as done in de Menezes et al., 2021) and use the best-fit values for the subsequent analysis.

We draw the TS profiles of each target by fitting the point source with 12 values of Γ between -0.5 and -5 and recording the corresponding TS value for each index. This profile peaks around the index value that maximizes the significance of the target, so in the case that the objects of a given sample indeed have similar spectral shapes, we should see an even taller peak near a specific value of Γ when summing or "stacking"all of its TS profiles. This stacked curve is denoted by $\mathrm{TS}_{\mathrm{stack}}$.

The TS amplitude of spurious fluctuations is taken into account by re-fitting each ROI again, this time without the main target but with a point source at a random location in the ROI. We do this 15 times for each ROI and draw TS profiles for the mock sources in the same way as our targets. In the end we have 2025 mock sources whose profiles we stack and normalize (divide by the number of mock sources per ROI, that is, 15) to produce $\mathrm{TS}_{\mathrm{noise}}$, a curve we interpret as the noise threshold for our population. This noise curve tells us how much better our modelling gets after we include point sources at random positions in the ROI. Since the TS is calculated by comparing two different hypothesis, we can play the same game and define a $\mathrm{TS}_{\mathrm{sample}}$ by subtracting the noise curve from the stacked profile:

$$\mathrm{TS}_{\mathrm{sample}} = \mathrm{TS}_{\mathrm{stack}} - \mathrm{TS}_{\mathrm{noise}} = 2\ln\left(\frac{L_{\mathrm{sample}}}{L_{\mathrm{noise}}}\right) \tag{3.2}$$

The maximum of this $\mathrm{TS}_{\mathrm{sample}}$ distribution will be our measure how much better our sample describes the *Fermi*-LAT observations than just spurious point sources. Therefore, even if we are not confident enough to claim any given target is an actual γ-ray source, by stacking the likelihoods of our dwarf AGN and comparing it with that of mock data we can say whether the collective emission from this population is consistent or not with the expectation from random fluctuations.

3.3 Variability analysis

Time variability is a common feature of AGN observed at all wavelengths, from optical to X-rays and γ-rays Peterson (2001). This variability can occur on time scales of a few minutes to years depending on the physics involved, even though the exact mechanisms responsible for it are not fully understood.

Our search for the flux variability of our best targets follows the procedure employed in Ajello et al. (2020) to identify AGN contamination to the γ-ray emission of their sample of

SF galaxies. We use the `lightcurve` method to generate light curves spanning the whole ~ 13 years of the LAT's 500 MeV−300 GeV observations. Because we have so few events attributable to our best targets (X17 and F14 have ~ 100 photons each) we divide the data into $n_b = 15$ bins covering ~ 11 months each.

The strength of a source's flux variability is measured by the quantity $\mathrm{TS}_{\mathrm{var}}$, which was defined in Nolan (2012) as is expressed in Equation 3.3, where $\mathcal{L}_i(\Phi_i)$ is the log-likelihood of the best-fit model where the target has photon flux Φ_i in the i-th time bin, and $\mathcal{L}_i(\Phi_{\mathrm{const}})$ the log-likelihood of the model where the target has constant flux over the entire dataset. The `lightcurve` method outputs $\mathrm{TS}_{\mathrm{var}}$, which we convert into a significance by assuming that under the null-hypothesis (no variability) the value of $\mathrm{TS}_{\mathrm{var}}$ is sampled from a chi-squared distribution with n_b degrees of freedom, like described in Nolan (2012).

$$\mathrm{TS}_{\mathrm{var}} = 2\sum_{i}^{n_b}[\mathcal{L}_i(\Phi_i) - \mathcal{L}_i(\Phi_{\mathrm{const}})] \tag{3.3}$$

If we have Z_1, ..., Z_k independent normally-distributed random variables with a mean of $\bar{Z}$, we can define the quantity $\chi^2_k = \sum_{i=1}^{k}(Z_i - \bar{Z})^2$. The value we obtain from this sum should then follow the so-called chi-squared distribution, represented by the probability density function $f_k(x)$ given in Equation 3.4; with $\Gamma(x) = (x-1)!$ denoting the gamma function. Examples of $f_k(x)$ for different values of k are shown in Figure 3.3. To determine if the Z variables are consistent with the expectation from sampling k normal distributions, one computes the probability of obtaining $x > \chi^2$ from $f_k(x)$ by doing $p = \int_{\chi^2}^{\infty} f_k(x)dx$. This quantity is called the p-value, and the smaller it is the less likely it is that the $Z_i - \bar{Z}$ differences arise from random fluctuations.

$$f_k(x) = \frac{x^{\frac{k}{2}-1}e^{-\frac{x}{2}}}{2^{\frac{k}{2}}\Gamma(\frac{k}{2})} \quad \text{, for } x > 0 \tag{3.4}$$

In our particular case, the null-hypothesis states that the fluxes of our targets are constant and that the differences $\mathcal{L}_i(\Phi_i) - \mathcal{L}_i(\Phi_{\mathrm{const}})$ in each time bin are simply due to random fluctuations. This is why $\mathrm{TS}_{\mathrm{var}}$ should follow a chi-squared distribution with n_b degrees of freedom. Under such conditions, in order for us to discard the null-hypothesis and claim these targets as variable on the time scale of a few years with a level of confidence of 99% ($p = 0.01$), we need our targets to display $\mathrm{TS}_{\mathrm{var}} = 30.6$.

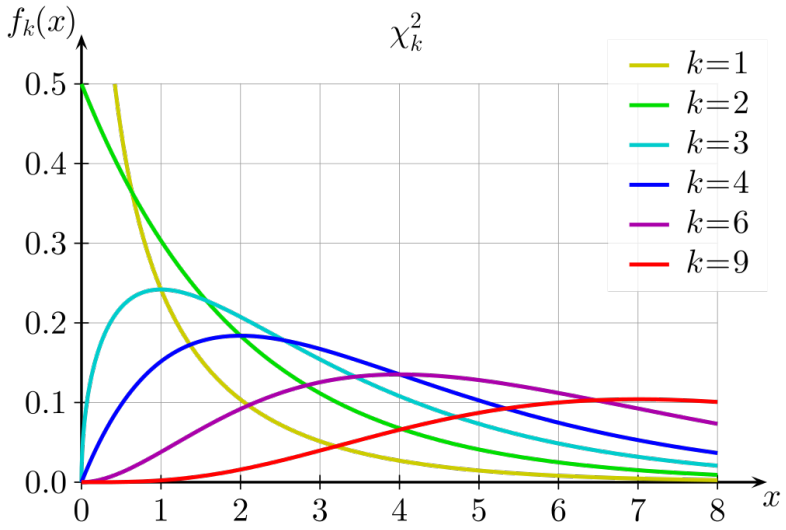

Figure 3.3: Plot of the chi-square distribution for different values of k. ©2010 Geek3 (`https://commons.wikimedia.org/wiki/User:Geek3`).

Chapter 4

Results

In this section we discuss the results from our analysis, including the output from `localize()` and the stacking procedure. Then we look for potential correlations involving the implied γ-ray luminosities of our targets with other observables that might hint towards the origin of the HE photon emission in our sample of dwarf AGN.

Running just our initial analysis resulted in 4 promising (TS > 9) γ-ray source candidates: X1, X17, F6 and F14. However, by taking a closer with the `localize()` function we found two of them (X1 and F6) had offsets between their original and TS peak positions exceeding the $r99$, meaning it's more likely their signal are just artifacts from an unmodeled nearby source or fluctuation (see Section 3.1 for details). This is shown in Figure 4.1. Including this nearby peak in the model and fitting again greatly reduces the TS of those targets to values < 4.

The other two (X17 and F14) were successfully localized in both energy intervals, as is shown in Figure 4.2. For F14 we find the original position sits almost perfectly on top of the TS peak, with an offset of merely $\delta = 0.03°$. This behaviour is seen in both energy intervals and increases our confidence that the observed signal is actually coming from that dwarf galaxy. After running `localize()` we get $\mathrm{TS}_{\mathrm{F14}} = 14$ and $r99 = 0.17°$ from the initial analysis. After including lower energy photons we get $\mathrm{TS}_{\mathrm{F14}} = 22$ and $r99 = 0.13°$, so the greater statistics have increased the significance and decreased the positional uncertainty of this candidate. Because of the small offsets and the consistency between both analyses we adopt the most optimistic TS value for this target. After `localize()`, X17 shows a decrease in TS in the new analysis in comparison with the original one, from 19.8 to 16.9; while the $r99$ increases from 0.27° to 0.35°, probably due to the large amount of low

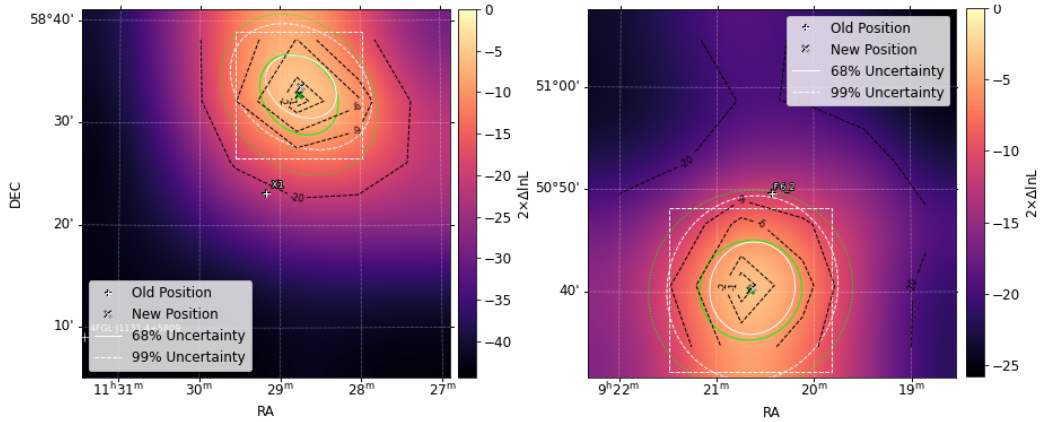

Figure 4.1: Zoom in on TS maps of regions surrounding failed attempts at localization: X1 (left) and F6 (right). The first failure occurred in the initial analysis (1 GeV − 300 GeV) while the second one only became noticeable after increasing the statistics available by extending the energy range (500 MeV − 300 GeV, see text). The color scale is the difference between the TS of a point source at that position and that of the peak, so that a point source at the peak represents a better fit to the data.

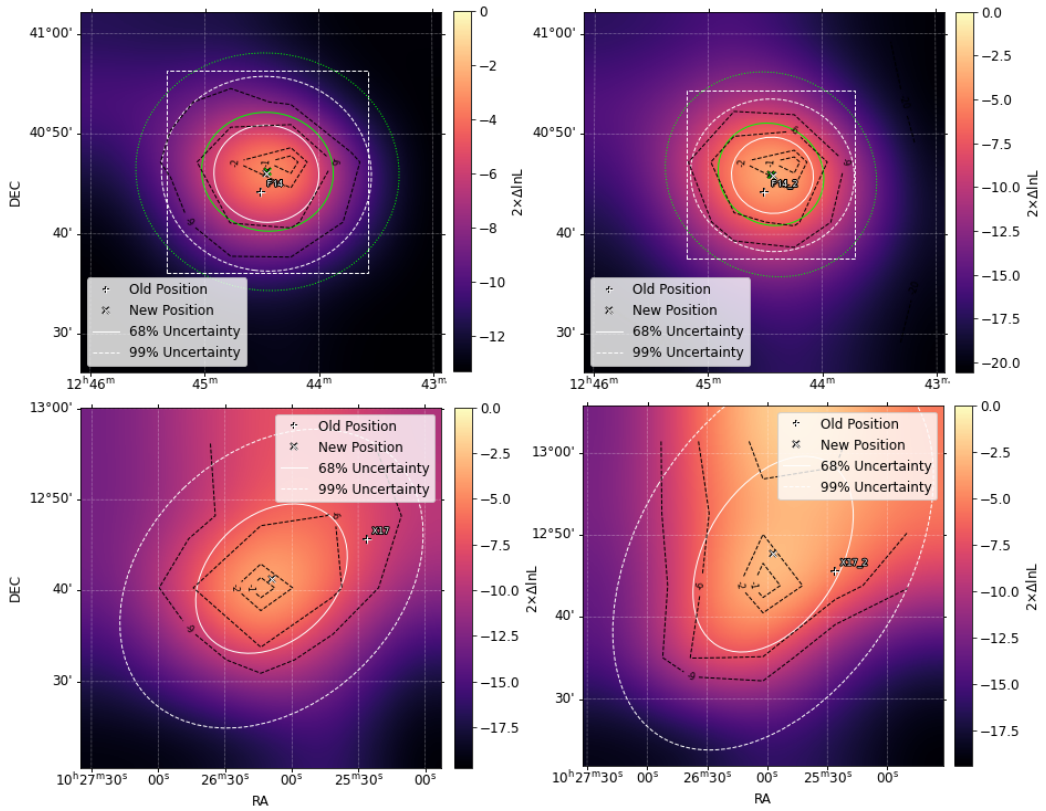

Figure 4.2: TS maps of the region surrounding each of the best γ-ray source candidates from the initial analysis: F14 (top) and X17 (bottom); results from the initial analysis (1 GeV − 300 GeV) are shown on the left column while the results from the extended analysis (500 MeV − 300 GeV) are on the right.

energy photons in this particularly noisy ROI. The new position given by the `localize()` method is also different in both analyses, with the offset between original and TS peak

positions $\delta = 0.19°$ dropping to $0.13°$ after including > 500 MeV photons. Faced with these disparate results, we chose to keep the more conservative TS value for this target.

One can check the γ-ray flux vs TS distribution of our targets after the initial analysis step on the left panel of Figure 4.3, where we also show the flux value of the weakest detected source in the 4FGL-DR2 (10 year) calatogue for comparison (about 4×10^{-13} erg/cm^2/s Ballet et al., 2020). As none of the targets pass the golden standard criteria of TS > 25, in the rest of this work we will only consider their 95% upper limit values when exploring the behavior of the γ-ray luminosities with respect to other observables. But we make exceptions for the two strongest candidates to get a sense of the scale of the emission of dwarf AGN implied by the LAT's observations. These are $L_\gamma^{\rm X17} = (1.39 \pm 0.59) \times 10^{42}$ and $L_\gamma^{\rm F14} = (3.68 \pm 1.78) \times 10^{41}$, with photon indexes $\Gamma_{\rm X17} = -2.45 \pm 0.24$ and $\Gamma_{\rm F14} = -2.28 \pm 0.26$.

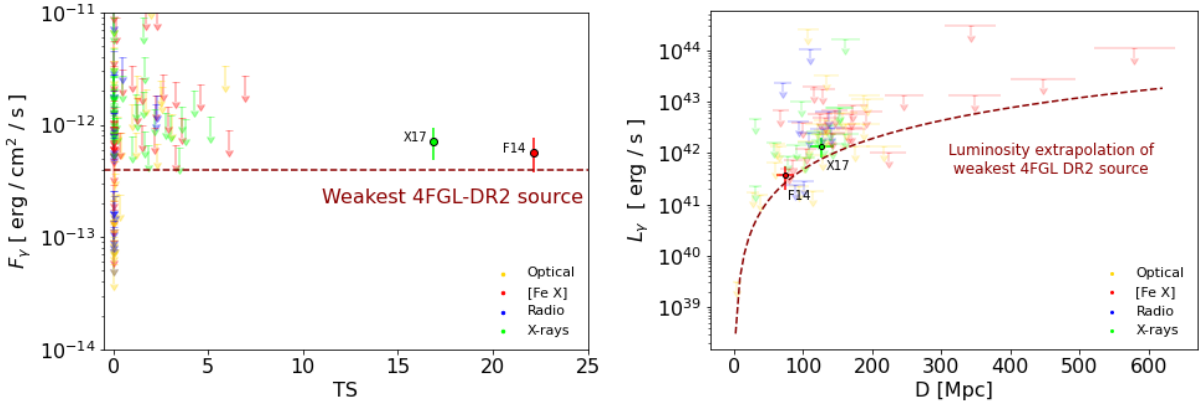

Figure 4.3: Left: γ-ray flux upper limits versus TS of individual targets. The strongest candidates for γ-ray emitting dwarf AGN are highlighted and plotted as their maximum-likelihood values. The dashed line corresponds to the flux value of the weakest detected 4FGL-DR2 source. Right: γ-ray luminosity upper limits versus host galaxy distance. The dashed line corresponds to the luminosity required for a detection with the *Fermi*-LAT at that distance (see text).

The right panel of Figure 4.3 shows L_γ vs distance distribution of our targets. Our dwarf AGN sample has redshifts in the $z \sim 0.01 - 0.14$ range ($D \sim 4.5 - 579$ Mpc), with a mean of $\bar{z} = 0.031$ ($\bar{D} = 129$ Mpc). By interpreting the flux of the weakest 4FGL source as a threshold for detection, we should only expect to find sources as bright as $L_\gamma = 10^{41}$ erg/s at distances smaller than ~ 50 Mpc from the Milky Way, and none fainter than 10^{42} erg/s that are beyond about 200 Mpc.

4.1 Stacking

Since no dwarf galaxies were detected at the 5σ level and most fail to reach even TS = 9, we have confirmation that our targets are indeed faint and difficult to separate from the background. The use of stacking analysis to study this undetected population is then justified.

The one-dimensional TS profiles over photon index space are shown in Figure 4.4. We draw the colored curves to represent the profiles of individual targets, while the black solid and dashed curves stand for the stacked and noise profiles respectively. The difference between these last two curves is plotted on the residual map, where we see our dwarf AGN sample has an excess of $TS_{AGN} = 36.2$ above the noise, corresponding to $\sim 6\sigma$, at the photon index value $\Gamma = -2.14$. So even though all objects in our sample are too faint to be detected individually, the data acquired by the *Fermi*-LAT favours the hypothesis of little monsters being γ-ray emitters by $\sim 6\sigma$ over the noise interpretation.

By employing the reasoning of comparing likelihoods exemplified in Equation 3.1 we can say the *Fermi*-LAT data favours the hypothesis of dwarf AGN as γ-ray sources over the noise by 72.5 million! It seems that AGN in dwarf galaxies are indeed significant γ-ray emitters even if all objects in our sample are too faint to be detected individually.

It is important to notice is how, because most targets fail to reach even TS = 9 (see Figure 4.3) the stacking is dominated by 2 moderate significance targets ($\sim 4\sigma$ each), F14 and X17, who constitute our strongest candidates for γ-ray emitting dwarf AGN.

The height of the stacked profile's peak and the similarity between the profiles of the 2 strongest candidates in Figure 4.4 indicates that our stacking hypothesis was justified after all, that is, our targets do have somewhat similar spectral shapes. Unfortunately, Γ alone does not give us enough information to tell *where* and *how* the γ-rays are being produced, so later in Section 5.1 we will discuss some possible origins of these HE photons.

One interesting thing we might do in the meantime is to check how the stacking results depend on each of the signatures used to detect the AGN. We divide our dwarf AGN population into the 4 sub-samples discussed in Chapter 2 and then stack them separately. This decomposition of the AGN sample is shown in Figure 4.5.

From this exercise we get TS excesses above the noise for the optical, X-ray and [Fe X] sub-samples of $TS_O = 9.7$, $TS_X = 13.1$ and $TS_F = 30.7$, but a slightly negative value

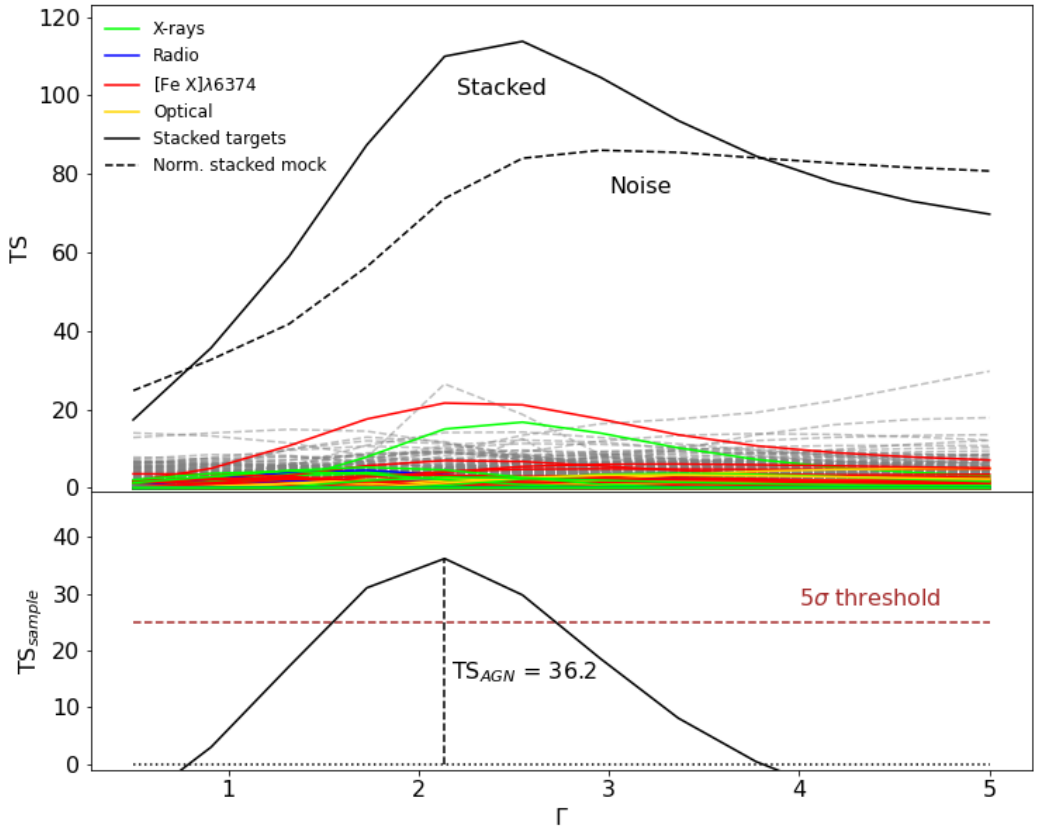

Figure 4.4: Individual and stacked 1D TS profiles for the dwarf AGN sample. Colored curves represent the TS profiles of individual targets, with the color standing for one of the detection signatures: yellow for optical narrow-line ratios consistent with AGN; red for [Fe X]λ6374 coronal line detection; blue for compact radio source incompatible with SF activity; green for X-ray detection. The black solid line corresponds to the stacked profile obtained from summing all individual AGN targets. Grey dashed lines are the profiles of the mock sources, while the black dashed curve represents the stacked noise normalized for the final sample. The residual plot traces the difference between the stacked and noise profiles.

for the radio one $\mathrm{TS_R} = -0.5$. So if we were basing our search for HE photons on any particular AGN feature, we would have found the [Fe X] sub-sample to be detected at the 5σ level, while the X-ray and optically selected populations would stay just above 3σ. Unfortunately, the signal from our radio sub-sample seems to be compatible with noise. In Section 5.2 we will discuss how dependent our results are on the best candidates, as well as point out problems with some of the radio-selected objects which calls into question their status as AGN candidates.

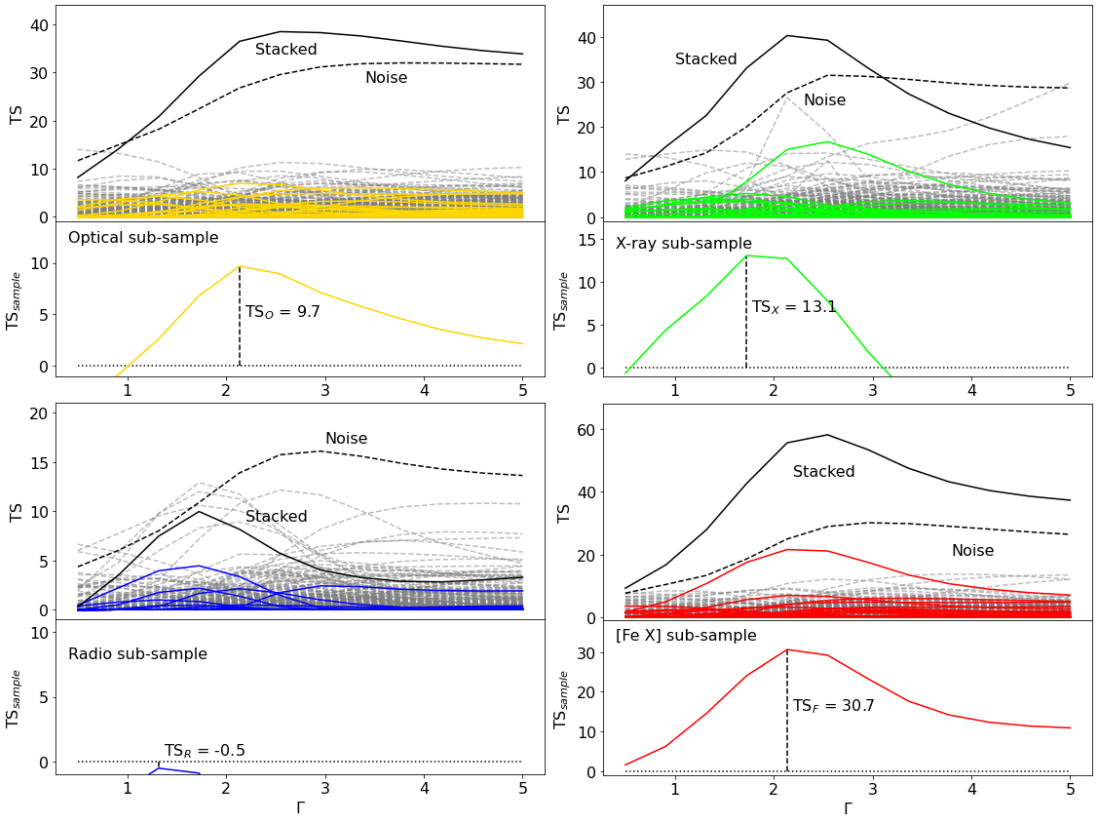

Figure 4.5: Individual and stacked 1D TS profiles decomposed into each of the 4 AGN samples. Targets that display multiple AGN indicators are included in all the samples they have a signature for. The colors and line scheme is the same used in Figure 4.4.

4.2 The control sample

We also apply our stacking technique to a control sample of non-AGN dwarf galaxies selected using optical diagnostics as described in Section 2.6. Just for comparison, we plot the line-ratio diagrams of both AGN (colored circles) and non-AGN (pink stars) dwarf galaxies in Figure 4.6.

We show the stacking this population Figure 4.7. The negative value of $\mathrm{TS_{SF}} = -0.1$ indicates how this control sample is no better at describing the observations than just spurious fluctuations. This fact suggests the presence of an active MBH is necessary in order to detect significant γ-ray emission from dwarf galaxies.

4.3 Light curves

The light curves of X17 and F14 are shown in the upper and lower panels of Figure 4.8 respectively. We plot the photon flux in the time bins where the targets were detected

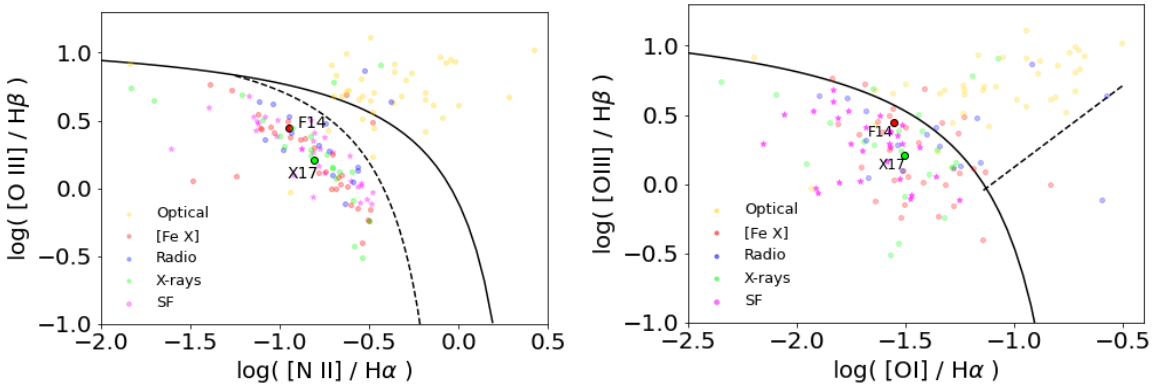

Figure 4.6: Optical narrow-line diagnostic diagrams for all 183 galaxies explored for γ-ray emission in this work. The demarcations separating SF and AGN regions as well as seyferts/LINERs are from Kewley et al. (2006).

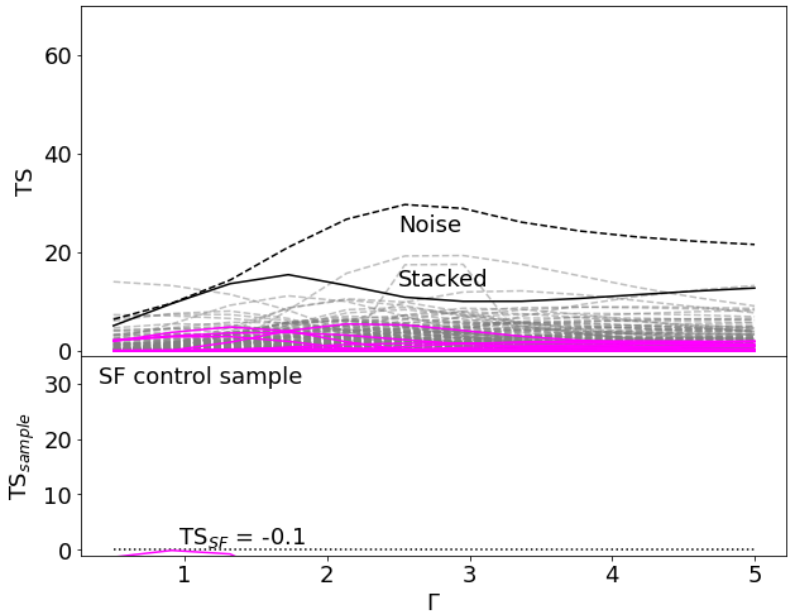

Figure 4.7: Individual and stacked 1D TS profiles of the control sample of SF galaxies. The line scheme is the same one used in Figure 4.4.

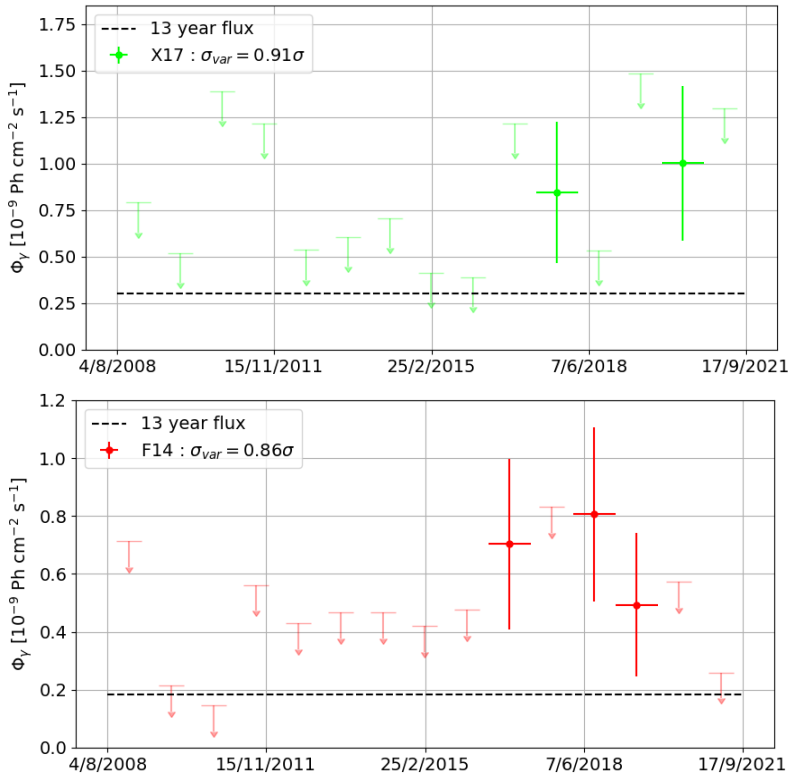

Figure 4.8: Light curves of our best candidates for γ-ray emitting dwarf AGN. The dashed lines indicate the fluxes averaged over the entire dataset. The data points show the photon flux in time bins in which the target reaches TS = 6, while the rest are the 95% upper limits.

with TS > 6, while using upper limits for the rest.

As was explained in Section 3.3, we need our targets to have $\mathrm{TS}_{\mathrm{var}} > 30.6$ so that we can say they are variable with a level of confidence of 99%. However, the values obtained for X17 and F14 are 15.2 and 14.8 respectively, corresponding to significances σ_{var} of only 0.91σ and 0.86σ. We conclude that our faint targets do not display evidence of variability on the scale of a few years. We could raise the number of bins in our analysis to look for variability on shorter time scales, but doing so would lower the number of events per bin and make the targets harder to detect in each time bin.

4.4 The L_γ−SFR relation

It can be difficult to separate the contributions of AGN and stellar activity to the overall observed luminosity of a galaxy in a given band of the electromagnetic spectrum. This is specially true for dwarf AGN since we expect the luminosity of all BHs to scale with

mass. This means the emission of actively accreting IMBHs may be hidden or significantly diluted by that of stellar processes. One avenue we explored to quantify the contribution of SF to the γ-ray emission of our dwarf targets is the $L_\gamma-$SFR relation.

In Ackermann (2012), using 3 years of *Fermi*-LAT data, they explore the γ-ray emission associated with SF activity in a sample of various types of galaxies, and find a correlation between L_γ and L_{IR} (at $8-1000\mu$m) spanning several orders of magnitude. The authors explain the link between L_{IR} and SFR can be understood by using the assumption that a significant portion of the UV photons produced by the massive and hot stars is absorbed by dust and then re-emitted in the IR, turning L_{IR} into a proxy for the amount of massive stars in that galaxy. Some of the cosmic rays (CRs) accelerated by the SNRs produced after this SF episode are expected to collide with nuclei in the interstellar gas and produce neutral pions π^0, which quickly decay into detectable MeV $-$ GeV photons. This work was later expanded on in Ajello et al. (2020) using 10 year data and a much larger sample.

In Kornecki et al. (2020) the $L_\gamma-$SFR relation is further investigated using the SFR calibrations of Kennicutt and Evans (2012):

$$\log(\mathrm{SFR}) = \log(L_{\mathrm{FUV}} + 3.89L_{25\mu m}) - 43.35 \tag{4.1}$$

$$\log(\mathrm{SFR}) = \log(L_{\mathrm{H}\alpha} + 0.02L_{25\mu m}) - 41.27 \tag{4.2}$$

where the luminosities are measured in erg/s and the SFR in $M_\odot/yr$.

Using a reduced data srt composed of only galaxies with inactive or dormant BHs they find the following relation with a scatter of 0.45 dex:

$$L_\gamma = 1.6 \times 10^{39} \left(\frac{\mathrm{SFR}}{M_\odot yr^{-1}}\right)^{1.38} \tag{4.3}$$

Although the energy range of the γ-rays analyzed in these works ($0.1-100$ GeV) is different than the one adopted for the present search, equation 4.3 still offers a useful order of magnitude reference for us to explore where our target dwarfs AGN are placed in comparison with the $L_\gamma-$SFR relation. We estimate the SFR for the dwarfs in all samples in the same way as done in Re20 and Mo21, where L_{FUV} is obtained from the Galaxy Evolution Explorer (GALEX) FUV flux measurements, while the W4 channel (22μm) from the All Wide-field Infrared Survey Explorer (ALLWISE) is used as a good approximation to the the 25μm flux, since the ratio of 22μm to 25μm flux densities is expected to be on the order of unity (see Jarrett, 2013). Whenever GALEX fluxes were not available we use the

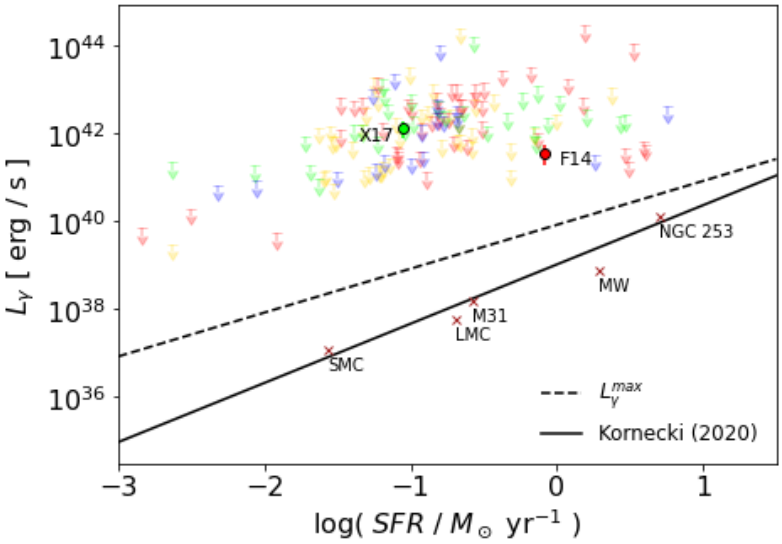

Figure 4.9: γ-luminosities as a function of SFR for dwarf AGN. Each detection signature is shown with a different color following the scheme outlined previously. The fit of Equation (4.3) is shown as the black solid line, together with the data of a few known galaxies plotted as little x's for reference. The calorimetric limit is also displayed as a dashed line.

Hα fluxes reported in the NSA and calculate the SFR as outlined in Equation 4.2.

The results from this exploration can be seen in Figure 4.9. We plot the fit from Kornecki et al. (2020) given by Equation 4.3 together with the data of a few galaxies cited in that work for reference, the dashed line corresponds to their prediction of the calorimetric limit ($L_\gamma^{\max} = 8.38 \times 10^{39}$SFR in erg/s as in equation 18 of Kornecki et al., 2020). This upper limit for the γ-ray brightness of a galaxy is derived by assuming that basically all of the CR luminosity from SF gets translated into γ-rays.

The large uncertainties associated with the low TS targets causes their respective 95% upper limits to fluctuate around 10^{39} - 10^{44} erg/s. For many of these weaker candidates the flux uncertainties are actually greater than their maximum-likelihood values.

On the other hand, the 2 strongest candidates have $L_\gamma^{\mathrm{X17}} = (1.39 \pm 0.59) \times 10^{42}$ and $L_\gamma^{\mathrm{F14}} = (3.68 \pm 1.78) \times 10^{41}$, which places them well above the expectation from their level of SF activity. To be more precise, if we adopt the scatter of $\sigma = 0.45$ dex for the fit of Equation 4.3 we conclude targets X17 and F14 lie around 10.3σ and 5.7σ above the relation. Although the complex interplay between CRs and the galaxy's ISM is difficult to model, this could be a hint another component is needed to explain the γ-ray output of these dwarfs besides stellar processes. Perhaps the AGN is to blame.

4.5 Proxies for AGN power

Another thing we can do to verify if the observed γ-ray signal is associated with our target dwarf AGN is to check the behaviour of L_γ with respect to changes in observables related MBH activity.

Because the 4 sub-samples were built using different AGN signatures, we use different proxies to study each of them: for the optical sample we use the [O III]λ5007 luminosity as derived from the Nasa Sloan Atlas (NSA) flux measurements, as it is one of the brightest emission lines observed in typical spectra of AGN and accounts for a large fraction of the energy budget from the NLR (Rawlings and Saunders, 1991; Celotti and Fabian, 1993). For the X-ray sample we use the 0.5-8 keV Chandra observations for the 10 objects from Bal 17 (O1-O10) and the 5 from Mo21 (O11, O12, R14, R15, R16), while using the 0.5-2 keV XMM data for the objects from Bi20 (O15, O45, X1-X30). For the radio sample we use the 1.4 GHz data from the FIRST Survey. Finally, for the [Fe X] sample we naturally default to the luminosity of the [Fe X]λ6374 coronal line as given in Mo21.

In Figure 4.10 we show the plots relating the L_γ upper limits to these different proxies and find no obvious correlation between them, but point out the apparent tendency of L_γ to increase with $L_{\mathbf{[Fe\ X]}}$ on the upper right panel.

To investigate this further we perform two tests designed to deal with regression in the presence of censored data (upper limits): the first is Cox's regression (Cox, 1972) available in the `ASURV` Fortran package, which when applied to our data gives a probability of $P_{Cox} = 0.85$ that no correlation exists between L_γ and $L_{\mathbf{[Fe\ X]}}$; and the second is the Akritas-Thiel-Sen (ATS) Kendall τ-rank correlation test (Feigelson and Babu, 2012) in the `NADA` R package, from which we get $\tau = 0.002$ and a probability $P_{\rm ATS} = 1$ of a non correlation. From the results of these tests there is no correlation between the two quantities. We note, however, how this is likely a consequence of the limitations of the available data, specially since we are dealing with a single actual data point (F14) while using upper limits for the weaker candidates.

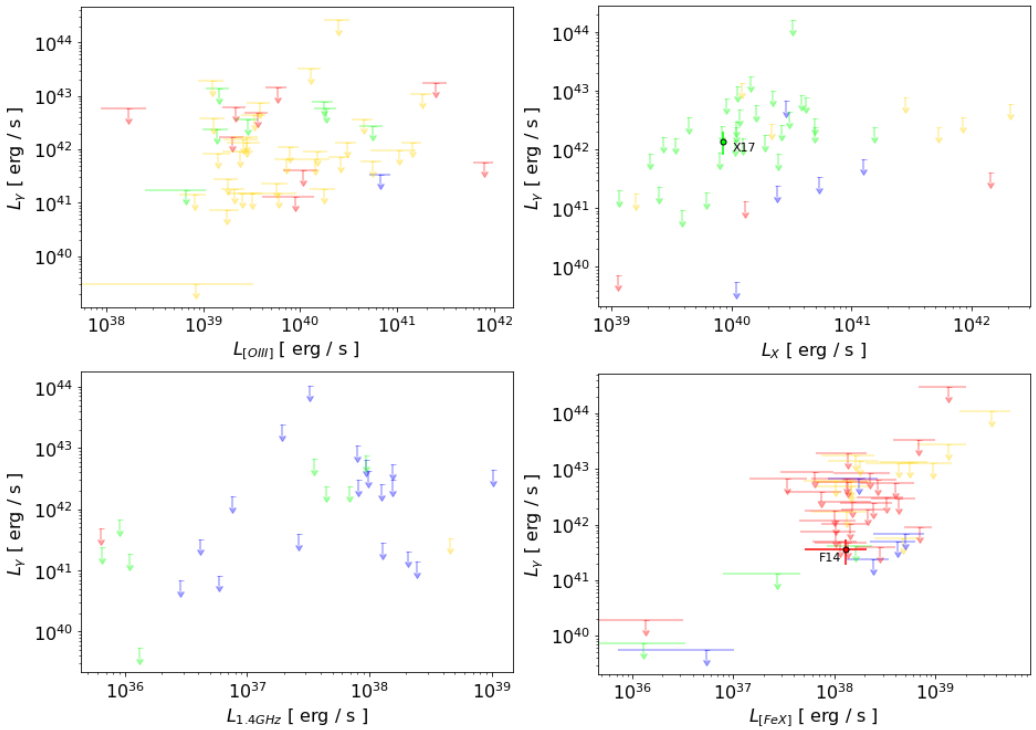

Figure 4.10: γ-ray luminosities as a function of proxies for AGN power for the 4 sub-samples (see text). Each sample is shown with a different color following the scheme outlined above.

Unfortunately the other proxies seem to correlate even less with the L_γ upper limits. Our targets are just too faint for us to draw strong conclusions about the physical origin of the HE photons using these relations.

Chapter 5

Discussion

In this chapter we will review our results and discuss the possible origin of the γ-ray emission while keeping in mind some important caveats involving both the sample and our analysis.

5.1 The origin of the γ-rays

By comparing the results from the stacking of the AGN and SF samples we have concluded that, although individual dwarf AGN may be faint γ-ray emitters they are still detected as a population, whereas similar dwarf galaxies that don't exhibit hints of an active MBH are not. This fact, together with the positions of our dwarf AGN relative to the $L_\gamma - SFR$ relation give good indication that the signal we are seeing is probably associated with the AGN and not with stellar activity, at least for the two strongest candidates. In Kornecki et al. (2020) they also discuss some outliers to the $L_\gamma - SFR$ relation that sit above the fit with γ-luminosities around $10^{39} - 10^{41}$ erg/s; these are NGC 2403, NGC 3424, NGC 4945, and the Circinus galaxy. Notably, all of them have hints of AGN activity that could be contributing to the γ-ray luminosity of their hosts (Gavazzi et al., 2011; Yaqoob, 2012; Yang et al., 2009; Peng et al., 2019).

We saw from the last chapter how our 2 strongest candidates have $L_\gamma^{\mathrm{F14}} = (3.68 \pm 1.78) \times 10^{41}$ erg/s and $L_\gamma^{\mathrm{X17}} = (1.39 \pm 0.59) \times 10^{42}$ erg/s. These values may seem large and indeed are about $10^2 - 10^3$ times the estimated γ-ray luminosity of the MW (see Strong, 2010); this correspond to about $1 - 10\%$ of the Eddington luminosity for BHs with masses between $10^5 - 10^6$ $\mathrm{M}_\odot$.

Unfortunately, we weren't able to constrain the origin of the γ-ray emission from dwarf

AGN by looking at how their luminosity upper limits behave in relation to other proxies for BH power. However, the apparent behaviour of the increasing L_γ upper limits with $L_{[\mathrm{Fe\ X}]}$ on the bottom-right panel of Figure 4.10 is tantalising enough to invite some speculation.

We have mentioned how the [Fe X]λ6374 coronal line was interpreted as arising from collisional excitation in jet-driven shocks in two different dwarf galaxies (Molina et al., 2021; Kimbro et al., 2021, our R11 and R15 respectively). This is the same conclusion reached in Rodríguez-Ardila and Fonseca-Faria (2020) by finding extended and blueshifted [Fe VII]λ6087 emission aligned with the ionization cones of the Circinus Galaxy. If shocks indeed contribute to the excitation of the CLR, it could lead to a correlation between the coronal line luminosity and that of γ-rays.

With only a single actual data point to plot in $L_\gamma - L_{[\mathrm{Fe\ X}]}$ space, it is difficult to say anything in favour or against the presence of a correlation between the two quantities. Regardless, we note that there are still 35 other dwarf galaxies displaying the [Fe X] coronal line in the sample of Mo21 left to be surveyed for γ-rays. Identifying additional strong γ-rays source candidates with [Fe X] lines could help clarify if there is a connection or if the apparent behaviour of the upper limits in Figure 4.10 is mere coincidence.

When it comes to RIAFs, a systematic search for the γ-ray emission of LLAGN was done in de Menezes et al. (2020) using 10 years of *Fermi* observations, but since only the radio-brightest sources were detected, the authors suggest the presence of jets might be more important for observing γ-rays than the RIAF component.

5.1.1 Jets

In the work of Nemmen et al. (2012), it was found that the same relation between jet power and γ-ray luminosity is followed by both blazars and gamma-ray bursts (GRBs) after correcting for the effect of beaming. This relation spans 10 orders of magnitude and suggests the existence of a common mechanism responsible for dissipating energy in BH jets, from those of GRBs to AGN, and possibly IMBHs. We are then tempted to check where our dwarf AGN fall with respect to this relation.

The jet power P_{jet} can be obtained from the radio luminosity in accordance with the correlation of Cavagnolo et al. (2010) between the mechanical power necessary to inflate the X-ray cavities observed in giant ellipticals and the jet radio emission, which we shown

in Equation 5.1.

$$P_{\rm jet} \simeq 5.8 \times 10^{43} \left(\frac{L_{\rm radio}}{10^{40} {\rm erg/s}} \right)^{0.7} {\rm erg/s} \tag{5.1}$$

This estimate was then found to correlate to the observed L_γ (uncorrected for beaming) of *Fermi* blazars as expressed in Equation 5.2 (see figure 1 of Nemmen et al., 2012). We note the weakest blazar of that work had $L_\gamma \sim 10^{43}$ erg/s, so we extrapolate the relation down to lower luminosities in order to compare it with our dwarf AGN.

$$\log(P_{\rm jet}) = 0.51 \log(L_\gamma) + 21.2 \tag{5.2}$$

We used Equation 5.1 to estimate the jet power from $L_{\rm radio}$ for objects in our sub-sample R. Since the rest of our dwarf AGN were not detected in radio, we relied on the upper limits for their 1.4 GHz emission available in the FIRST[1] catalogue (typically ~ 1.5 mJy) to obtain upper limits for their jet power $P_{\rm jet}^{\rm UL}$. All of our dwarf AGN are plotted in Figure 5.1 as upper limits in L_γ, with the exception of F14 and X17.

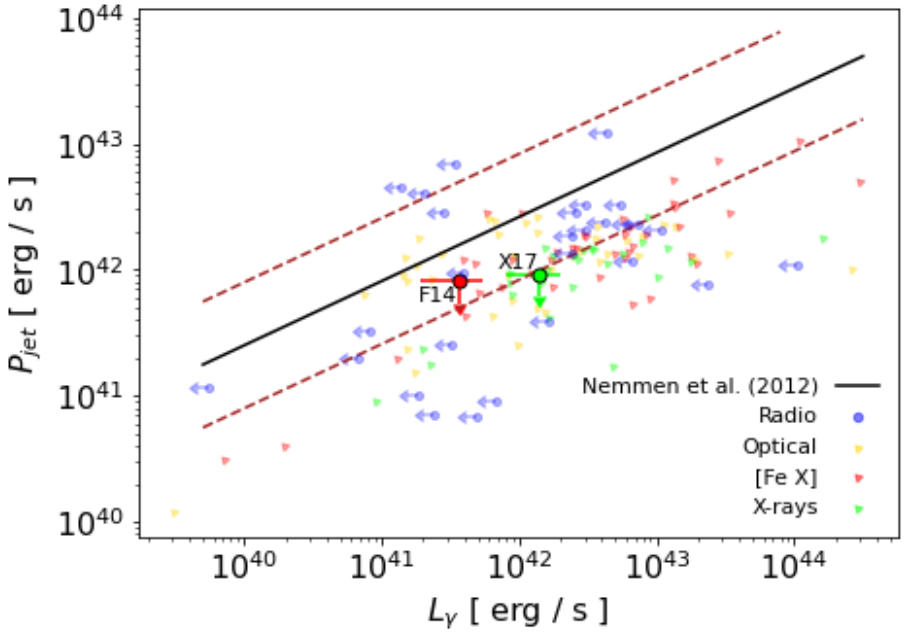

Figure 5.1: Jet power versus γ-ray luminosities. Our strongest candidates are highlighted and plotted as their upper limits for $P_{\rm jet}$, while the radio sub-sample is plotted as upper limits for L_γ. All other points are upper limits for both $P_{\rm jet}$ and L_γ. We extrapolate the relation of Equation 5.2 to luminosities lower than 10^{43} erg/s and show it as the solid line, and the scatter of 0.5 dex as the dashed lines.

Our estimates of $P_{\rm jet}^{\rm UL}$ for the two strongest candidates are around $\sim 10^{42}$ erg/s, about

[1] `http://sundog.stsci.edu/index.html`

one order of magnitude above the expectation set by the BZ mechanism for a maximally-rotating $10^5 M_\odot$ BH (Equation 1.3); alternatively, the same jet powers could be reached by a $10^6 M_\odot$ BH tangled in a magnetic field of $B \gtrsim 3 \times 10^4$ G. It therefore seems plausible that the γ-ray emission of our dwarf AGN could have its origin in undetected jets.

If these objects indeed have jets and if these jets happened to be aligned with our line of sight, it would beam their radiation towards us and make them easier to spot. This would also make our targets the first "dwarf-blazars"ever found. Beamed AGN often display flux variability on time scales of minutes to even years, so we have checked for this possibility by analysing the light curves of our best candidates (see Section 4.3). The γ-ray fluxes of our targets were not found to be significantly variable ($\sigma_{\rm var} \sim 0.9\sigma$) on the time scale of a few years, and unfortunately they are too faint for us to investigate their variability on shorter time scales.

The lack of radio detections to accompany the [Fe X] line in F14 and the X-ray emission of X17 means we are unable to confidently assert the γ-rays from these galaxies come from jets. Deeper radio observations will be needed to constrain the nature of the HE activity of our dwarf AGN.

5.2 Caveats and detectability

We saw how the stacking is dominated by the contribution of the two best candidates for γ-ray emitting dwarf AGN. One question we might then ask is how dependent the stacking results are on these candidates. In other words, if their signal is not associated with the dwarf AGN how would it affect the significance for the rest our sample?

The average noise was accounted for by us fitting many mock sources, but since our targets usually have arcsecond-scale sizes, the relatively large positional uncertainties ($r99 \sim 0.1^\circ$) leave open the possibility that a close background source or particularly bright fluctuation is responsible for the signal of our strongest candidates. This is specially true for X17, which has a larger offset between galaxy and peak TS positions even though it is still inside the $r99$ (see Figure 4.2).

If we exclude any one of the best candidates from the stacking the resulting $\mathrm{TS_{AGN}}$ from Figure 4.4 will drop to the range of 15 to 23.5 depending on which one we choose, F14

or X17. This means the significance of γ-ray from the rest of the sample would be around $3.8 - 4.8\sigma$, which would still be an interesting excess but not a detection. If instead both candidates prove unreliable we would be left with $\mathrm{TS_{AGN}} = 6.1$, or with a significance of only 2.4σ. The residual TS profiles after each exclusion are shown below in Figure 5.2. Doing the same for sub-samples X and F yields $\mathrm{TS_X} = 6.7$ and $\mathrm{TS_F} = 9.5$, so both sub-samples would be left with moderate $2.5-3\sigma$ excesses above the noise; just like sub-sample O with its 3.1σ, which did not had any strong candidates to begin with. We show the residual TS profiles of these sub-samples in Figure 5.3.

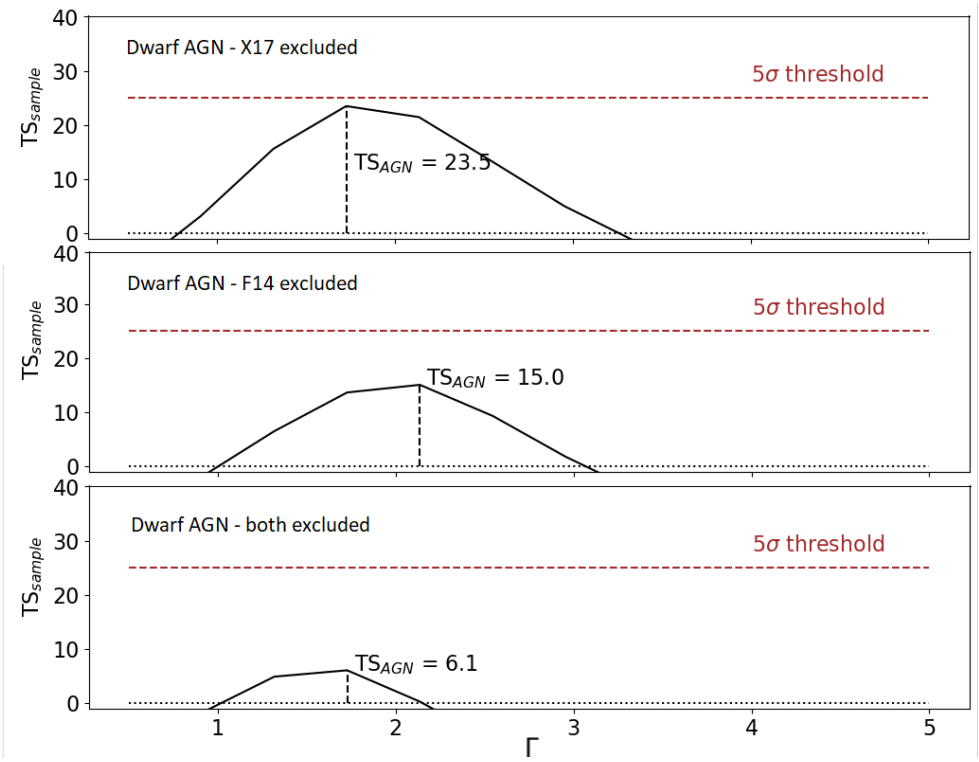

Figure 5.2: Residual $\mathrm{TS_{AGN}}$ profiles after excluding our best candidates. Top: excluding target X17. Middle: excluding target F14. Bottom: excluding both.

With only 28 objects, the radio sub-sample is the smallest and least significant of the 4. In a recent work, Sargent et al. (2022), the authors reanalyse the 13 best radio AGN candidates from Re20 (our R1-R13) using the greater resolution of the Very Long Baseline Array (VLBA), and find that the 4 compact sources that were detected (R1, R3, R5 and R8) had brightness temperatures $T_b > 10^6$ K consistent with MBH activity but are also the most offset $\gtrsim 2.5 - 5$" away from their host's center. They point out how these could be wandering MBHs or, more likely, background AGN unrelated to the targeted dwarf

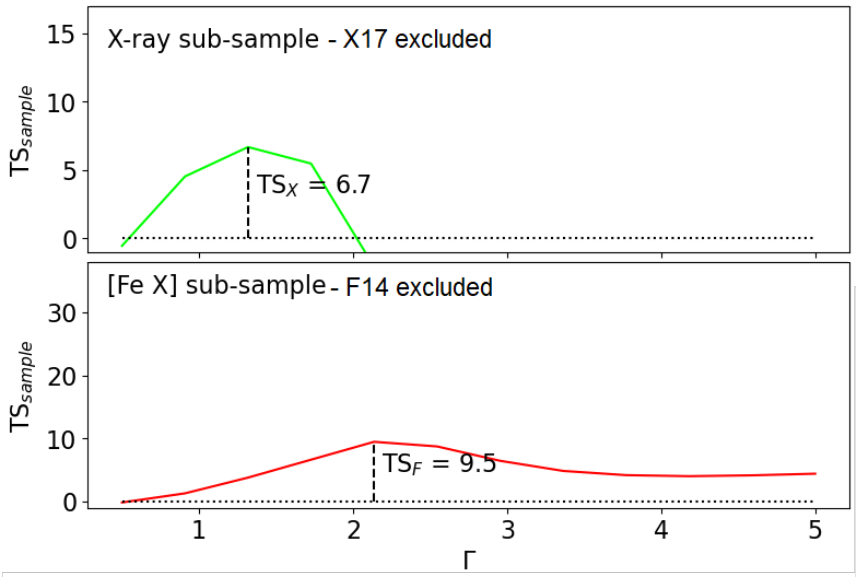

Figure 5.3: Residual TS profiles of sub-samples X and F after excluding our best candidates. Top: X-ray sub-sample. Bottom: [Fe X] sub-sample.

galaxies. The other 9 non-detections had a significant fraction of the flux density extended beyond the angular scale detectable with the VLBA ($\sim$ 30 mas) as well as brightness temperatures consistent with the SF scenario.

Given all of the caveats involving half of sub-sample R, it may not be surprising that we see no significant TS excess from its stacking on the bottom-left panel of Figure 4.5.

Chapter 6

Conclusions

We have used over 13 years of data gathered by the *Fermi*-LAT to look for the γ-rays from a population of dwarf galaxies displaying evidence of MBH activity. All targets are too faint to warrant individual detections, so we have performed a stacking analysis of our sample in order to probe its collective γ-ray emission properties. In summary, our findings include:

- Stacking the dwarf AGN sample results in a TS peak above the noise of $\mathrm{TS_{AGN}} = 36.2$ (a significance of $\sim 6\sigma$) at the photon index value $\Gamma = -2.14$. This stacking is dominated by the contribution of 2 moderate significance candidates, F14 and X17, both of which are found to sit around the 4σ confidence level. Of these two, we consider F14 to be the most promising candidate, as this dwarf galaxy sits right on top of the maximum of its spatial TS distribution.
- Dividing the AGN sample in accordance with the electromagnetic signatures used to identify the MBH results in 4 sub-samples with some overlap: O, X, R and F. These display TS excesses above the noise of $\mathrm{TS_O} = 9.7$, $\mathrm{TS_X} = 13.1$, $\mathrm{TS_R} = -0.5$ and $\mathrm{TS_F} = 30.7$ respectively. This means that if we were basing our search for HE photons on any particular MBH feature, we would have found the [Fe X] sub-sample to be detected at the 5σ level, while the X-ray and optically selected objects would stay just above 3σ. The signal from the radio sub-sample seems compatible with noise, but we believe this is a problem with the objects which constitute this particular sample and not evidence for a disconnect between jets and γ-rays in dwarf AGN.
- We explored the dependence of the stacking results on targets F14 and X17 by

excluding their contribution from the stacking. This resulted in TS_{AGN} decreasing to values of $15 - 23$, which correspond to a significance of $3.8 - 4.8\sigma$ for the γ-ray emission of dwarf AGN. Doing the same for the stacking of the sub-samples yields $2.5 - 3.1\sigma$ significances for all the MBH signatures, with the exception of radio.

- The stacking of a control sample of similar dwarf galaxies that otherwise show no evidence for an active nucleus results in a TS peak of $TS_{SF} = -0.1$, which smaller than all AGN sub-samples with the exception of sample R. This suggests the presence of an active MBH is necessary in order to find γ-ray emission from dwarf galaxies.
- Comparing the L_γ of the two highest TS targets with the expectation from their level of SF activity as predicted by the $L_\gamma-$ SFR relation reveals that both candidates are far too bright ($L_\gamma \sim 10^{41.5} - 10^{42}$ erg/s) to be explained by stellar processes alone. We believe the AGN is the natural explanation for this excess.
- We explored the behavior of the L_γ 95% upper limits in relation to different proxies for AGN power but did not find anything interesting, except for the vague tendency of increasing L_γ with $L_{[\mathbf{Fe\ X}]}$. Two tests were performed to check the validity of this apparent behavior and both returned null results, possibly due to the low number of points. Further exploration of the γ-ray emission from coronal-line emitting objects is needed to to fully exclude the possibility of a correlation between these quantities.
- We have analysed the light curves of our best targets and found no evidence for variability of their γ-ray flux on time scales of a few years.
- We estimate upper limits for the jet powers of our dwarf AGN which lack radio detections. The values of $P_{\rm jet}^{\rm UL}$ found for our best candidates are consistent with a jet origin for the γ-rays, perhaps even a beamed one. Deeper radio observations are necessary in order to say whether these systems have so far undetected jets.

It seems that even if we were to be very pessimistic about our findings and assume both F14 and X17 to be flukes, our hypothesis that active MBHs in dwarf galaxies are γ-ray emitters is still favored by the data over the spurious sources interpretation at the 2.4σ level. This means our hypothesis is, at the very least $\sim 18\times$ more likely than the null (see Equation 3.1), a result that holds even when analysing each sub-sample separately (with the exception of radio).

Our strongest candidate for γ-ray emitting dwarf AGN (F14) was identified as an AGN system solely by the presence of the [Fe X] line in its spectrum. Taking this together with the fact that sub-sample F is the most significant of the 4, raises our confidence about the potential of using the [Fe X]λ6374 line (and possibly other coronal lines) to detect active MBHs. Furthermore, a connection between γ-rays and coronal line emission could be a hint of the presence of AGN-driven outflows in these dwarfs, either in form of jets or spherical winds. If this is the case, it would have implications for the role of AGN feedback in dwarf galaxies and the evolution of large-scale structure in the Universe, as we have pointed out in Section 1.1.1.

We have not been able to constrain the nature of the γ-ray activity from the objects we analysed, but we note how their luminosity scale is compatible with the estimate of the Blandford-Znajek jet power for $10^5 - 10^6 M_\odot$ black holes. Additionally, if beaming effects are responsible for amplifying their emission, our best candidates would constitute the first dwarf-blazars ever found. Unfortunately, their faintness makes it difficult to asses this possibility by looking at their γ-ray variability. Therefore future radio observations of F14 and X17 are essential to constrain the jet power (if they have jets) and help us clarify the origin of their γ-ray emission.

Bibliography

Ackermann M. e., GeV Observations of Star-forming Galaxies with the Fermi Large Area Telescope, ApJ, 2012, vol. 755, p. 164

Aihara H., The Eighth Data Release of the Sloan Digital Sky Survey: First Data from SDSS-III, ApJS, 2011, vol. 193, p. 29

Ajello M., Gamma Rays from Fast Black-hole Winds, The Astrophysical Journal, 2021, vol. 921, p. 144

Ajello M., Di Mauro M., Paliya V. S., Garrappa S., The γ-Ray Emission of Star-forming Galaxies, ApJ, 2020, vol. 894, p. 88

ATLAS Collaboration. Observation of a new particle in the search for the Standard Model Higgs boson with the ATLAS detector at the LHC, Physics Letters B, 2012, vol. 716, p. 1

Atwood W. B., THE LARGE AREA TELESCOPE ON THE *FERMI GAMMA-RAY SPACE TELESCOPE* MISSION, The Astrophysical Journal, 2009, vol. 697, p. 1071

Baldassare V. F., Reines A. E., Gallo E., Greene J. E., X-ray and Ultraviolet Properties of AGNs in Nearby Dwarf Galaxies, ApJ, 2017, vol. 836, p. 20

Baldwin J. A., Phillips M. M., Terlevich R., Classification parameters for the emission-line spectra of extragalactic objects., PASP, 1981, vol. 93, p. 5

Ballet J., Burnett T. H., Digel S. W., Lott B., , 2020 Fermi Large Area Telescope Fourth Source Catalog Data Release 2

Bañados E., An 800-million-solar-mass black hole in a significantly neutral Universe at a redshift of 7.5, Nature, 2017, vol. 553, p. 473

Barai P., de Gouveia Dal Pino E. M., Intermediate-Mass Black Hole Feedback in Dwarf Galaxies: a View from Cosmological Simulations, Proceedings of the International Astronomical Union, 2018, vol. 14, p. 154

Barai P., de Gouveia Dal Pino E. M., Intermediate-mass black hole growth and feedback in dwarf galaxies at high redshifts, Monthly Notices of the Royal Astronomical Society, 2019, vol. 487, p. 5549

Bellovary J., Volonteri M., THE FIRST MASSIVE BLACK HOLE SEEDS AND THEIR HOSTS, The Astrophysical Journal, 2011, vol. 742, p. 13

Bellovary J. M., Cleary C. E., Munshi F., Tremmel M., Christensen C. R., Brooks A., Quinn T. R., Multimessenger signatures of massive black holes in dwarf galaxies, Monthly Notices of the Royal Astronomical Society, 2018, vol. 482, p. 2913

Bentz M. C., The Low-luminosity End of the Radius-Luminosity Relationship for Active Galactic Nuclei, ApJ, 2013, vol. 767, p. 149

Berk D. E. V., Richards G. T., Bauer A., Strauss M. A., Schneider D. P., Heckman T. M., York D. G., Hall P. B., Fan X., Composite Quasar Spectra from the Sloan Digital Sky Survey, The Astronomical Journal, 2001, vol. 122, p. 549

Biller B. A., Jones C., Forman W. R., Kraft R., Ensslin T., Hot Gas Structure in the Elliptical Galaxy NGC 4472, The Astrophysical Journal, 2004, vol. 613, p. 238

Birchall K. L., Watson M. G., Aird J., X-ray detected AGN in SDSS dwarf galaxies, MNRAS, 2020, vol. 492, p. 2268

Blandford R. D., Znajek R. L., Electromagnetic extraction of energy from Kerr black holes., MNRAS, 1977, vol. 179, p. 433

Bose S., Hellwing W. A., Frenk C. S., Jenkins A., Lovell M. R., Helly J. C., Li B., Gonzalez-Perez V., Gao L., Substructure and galaxy formation in the Copernicus Complexio warm dark matter simulations, Monthly Notices of the Royal Astronomical Society, 2016, vol. 464, p. 4520

Böttcher M., Reimer A., Sweeney K., Prakash A., LEPTONIC AND HADRONIC MODELING OF *FERMI*-DETECTED BLAZARS, The Astrophysical Journal, 2013, vol. 768, p. 54

Boylan-Kolchin M., Bullock J. S., Kaplinghat M., Too big to fail? The puzzling darkness of massive Milky Way subhaloes, Monthly Notices of the Royal Astronomical Society: Letters, 2011, vol. 415, p. L40

Cann J. M., Satyapal S., Abel N. P., Blecha L., Mushotzky R. F., Reynolds C. S., Secrest N. J., The Limitations of Optical Spectroscopic Diagnostics in Identifying Active Galactic Nuclei in the Low-mass Regime, The Astrophysical Journal, 2019, vol. 870, p. L2

Caproni A., Lanfranchi G. A., Baio G. H. C., Kowal G., Falceta-Gonç alves D., Gas Removal in the Ursa Minor Galaxy: Linking Hydrodynamics and Chemical Evolution Models, The Astrophysical Journal, 2017, vol. 838, p. 99

Caproni A., Lanfranchi G. A., da Silva A. L., Falceta-Gonç alves D., THREE-DIMENSIONAL HYDRODYNAMICAL SIMULATIONS OF THE SUPERNOVAE-DRIVEN GAS LOSS IN THE DWARF SPHEROIDAL GALAXY URSA MINOR, The Astrophysical Journal, 2015, vol. 805, p. 109

Carigi L., Colin P., Peimbert M., Sarmiento A., Chemical Evolution of Irregular and Blue Compact Galaxies, ApJ, 1995, vol. 445, p. 98

Cavagnolo K. W., McNamara B. R., Nulsen P. E. J., Carilli C. L., Jones C., Bîrzan L., A RELATIONSHIP BETWEEN AGN JET POWER AND RADIO POWER, The Astrophysical Journal, 2010, vol. 720, p. 1066

Celotti A., Fabian A. C., The kinetic power and luminosity of parsec-scale radio jets â an argument for heavy jets, Monthly Notices of the Royal Astronomical Society, 1993, vol. 264, p. 228

Choudhury T. R., Ferrara A., Gallerani S., On the minimum mass of reionization sources, Monthly Notices of the Royal Astronomical Society: Letters, 2008, vol. 385, p. L58

Cicone C., Massive molecular outflows and evidence for AGN feedback from CO observations, A&A, 2014, vol. 562, p. A21

Condon J. J., Radio emission from normal galaxies., ARA&A, 1992, vol. 30, p. 575

Cox D. R., Regression Models and Life-Tables, Journal of the Royal Statistical Society., 1972, vol. SeriesB (Methodological), 34, p. 187

Croom S. M., Smith R. J., Boyle B. J., Shanks T., Miller L., Outram P. J., Loaring N. S., The 2dF QSO Redshift Survey â XII. The spectroscopic catalogue and luminosity function, Monthly Notices of the Royal Astronomical Society, 2004, vol. 349, p. 1397

Dashyan G., Silk J., Mamon G. A., Dubois Y., Hartwig T., AGN feedback in dwarf galaxies?, Monthly Notices of the Royal Astronomical Society, 2017, vol. 473, p. 5698

de Blok W. J. G., The Core-Cusp Problem, Advances in Astronomy, 2010, vol. 2010, p. 789293

de Menezes R., Nemmen R., Finke J. D., Almeida I., Rani B., Gamma-ray observations of low-luminosity active galactic nuclei, Monthly Notices of the Royal Astronomical Society, 2020, vol. 492, p. 4120

de Menezes R., Orlando E., Di Mauro M., Strong A., A study of superluminous stars with the Fermi-Large Area Telescope, MNRAS, 2021, vol. 507, p. 680

De Robertis M. M., Osterbrock D. E., An analysis of the narrow-line profiles in high ionization Seyfert galaxies., ApJ, 1984, vol. 286, p. 171

Dermer C. D., Giebels B., Active galactic nuclei at gamma-ray energies, Comptes Rendus Physique, 2016, vol. 17, p. 594

Dong X.-B., Ho L. C., Yuan W., Wang T.-G., Fan X., Zhou H., Jiang N., A UNIFORMLY SELECTED SAMPLE OF LOW-MASS BLACK HOLES IN SEYFERT 1 GALAXIES, The Astrophysical Journal, 2012, vol. 755, p. 167

Drinkwater M. J., Gregg M. D., Hilker M., Bekki K., Couch W. J., Ferguson H. C., Jones J. B., Phillipps S., A class of compact dwarf galaxies from disruptive processes in galaxy clusters, Nature, 2003, vol. 423, p. 519

Elbert O. D., Bullock J. S., Garrison-Kimmel S., Rocha M., Oñorbe J., Peter A. H. G., Core formation in dwarf haloes with self-interacting dark matter: no fine-tuning necessary, Monthly Notices of the Royal Astronomical Society, 2015, vol. 453, p. 29

Erkens U., Appenzeller I., Wagner S., VizieR Online Data Catalog: Nature of the FHIL winds from AGN (Erkens+ 1997), VizieR Online Data Catalog, 1997, pp J/A+A/323/707

Fan X., A Survey of $z > 5.8$ Quasars in the Sloan Digital Sky Survey. I. Discovery of Three New Quasars and the Spatial Density of Luminous Quasars at $z \sim 6$, The Astronomical Journal, 2001, vol. 122, p. 2833

Fan X., Evolution of high-redshift quasars, New Astronomy Reviews, 2006, vol. 50, p. 665

Feigelson E. D., Babu G. J., Modern Statistical Methods for Astronomy: With R Applications. Cambridge University Press, 2012

Fernandes R. C., Stasiń ska G., Mateus A., Asari N. V., A comprehensive classification of galaxies in the Sloan Digital Sky Survey: how to tell true from fake AGN?, Monthly Notices of the Royal Astronomical Society, 2011, vol. 413, p. 1687

Filippenko A. V., Sargent W. L. W., Discovery of an Extremely Low Luminosity Seyfert 1 Nucleus in the Dwarf Galaxy NGC 4395, ApJ, 1989, vol. 342, p. L11

Finke J. D., Dermer C. D., Böttcher M., Synchrotron Self-Compton Analysis of TeV X-Ray-Selected BL Lacertae Objects, The Astrophysical Journal, 2008, vol. 686, p. 181

Gallazzi A., Charlot S., Brinchmann J., White S. D. M., Tremonti C. A., The ages and metallicities of galaxies in the local universe, MNRAS, 2005, vol. 362, p. 41

Gavazzi G., Savorgnan G., Fumagalli M., The complete census of optically selected AGNs in the Coma supercluster: the dependence of AGN activity on the local environment, A&A, 2011, vol. 534, p. A31

Gawiser E., , 2005 Galaxy Formation

Geha M., Blanton M. R., Yan R., Tinker J. L., A Stellar Mass Threshold for Quenching of Field Galaxies, ApJ, 2012, vol. 757, p. 85

Gofford J., Reeves The Suzaku view of highly ionized outflows in AGN â I. Statistical detection and global absorber properties, Monthly Notices of the Royal Astronomical Society, 2013, vol. 430, p. 60

Governato F., Colpi M., Maraschi L., The fate of central black holes in merging galaxies, Monthly Notices of the Royal Astronomical Society, 1994, vol. 271, p. 317

Greene J. E., Low-mass black holes as the remnants of primordial black hole formation, Nature Communications, 2012, vol. 3

Greene J. E., Ho L. C., Active Galactic Nuclei with Candidate Intermediate-Mass Black Holes, The Astrophysical Journal, 2004, vol. 610, p. 722

Greene J. E., Ho L. C., Estimating Black Hole Masses in Active Galaxies Using the Hα Emission Line, ApJ, 2005, vol. 630, p. 122

Greene J. E., Ho L. C., A New Sample of Low-Mass Black Holes in Active Galaxies, The Astrophysical Journal, 2007, vol. 670, p. 92

Greene J. E., Strader J., Ho L. C., Intermediate-Mass Black Holes, Annual Review of Astronomy and Astrophysics, 2020, vol. 58, p. 257

Greenstein J. L., Matthews T. A., Redshift of the Radio Source 3C 48., AJ, 1963, vol. 68, p. 279

Groves B. A., Heckman T. M., Kauffmann G., Emission-line diagnostics of low-metallicity active galactic nuclei, Monthly Notices of the Royal Astronomical Society, 2006, vol. 371, p. 1559

Gunn J. E., On the Distances of the Quasi-Stellar Objects, ApJ, 1971, vol. 164, p. L113

Haardt F., Maraschi L., A Two-Phase Model for the X-Ray Emission from Seyfert Galaxies, ApJ, 1991, vol. 380, p. L51

Haiman Z., The Formation of the First Massive Black Holes. In The First Galaxies , vol. 396 of Astrophysics and Space Science Library, 2013, p. 293

Harris D. E., Carilli C. L., Perley R. A., X-ray emission from the radio hotspots of Cygnus A, Nature, 1994, vol. 367, p. 713

Ho L. C., , 2003 The Central Engines of Low-Luminosity AGNs

Ho L. C., "Low-State" Black Hole Accretion in Nearby Galaxies, Ap&SS, 2005, vol. 300, p. 219

Ho L. C., Nuclear Activity in Nearby Galaxies, Annual Review of Astronomy and Astrophysics, 2008, vol. 46, p. 475

Ho L. C., RADIATIVELY INEFFICIENT ACCRETION IN NEARBY GALAXIES, The Astrophysical Journal, 2009, vol. 699, p. 626

Ho L. C., Filippenko A. V., Sargent W. L. W., A Search for "Dwarf" Seyfert Nuclei. III. Spectroscopic Parameters and Properties of the Host Galaxies, ApJS, 1997, vol. 112, p. 315

Hodge P. W., Dwarf Galaxies, Annual Review of Astronomy and Astrophysics, 1971, vol. 9, p. 35

Holberg J. B., Sirius B and the Measurement of the Gravitational Redshift, Journal for the History of Astronomy, 2010, vol. 41, p. 41

Ichimaru S., Bimodal behavior of accretion disks: theory and application to Cygnus X-1 transitions., ApJ, 1977, vol. 214, p. 840

Jarrett T. H., Extending the Nearby Galaxy Heritage with WISE: First Results from the WISE Enhanced Resolution Galaxy Atlas, AJ, 2013, vol. 145, p. 6

Keller B. W., Wadsley J., Couchman H. M. P., Cosmological galaxy evolution with super-bubble feedback â II. The limits of supernovae, Monthly Notices of the Royal Astronomical Society, 2016, vol. 463, p. 1431

Kennicutt Robert C. J., Star Formation in Galaxies Along the Hubble Sequence, ARA&A, 1998, vol. 36, p. 189

Kennicutt R. C., Evans N. J., Star Formation in the Milky Way and Nearby Galaxies, ARA&A, 2012, vol. 50, p. 531

Kewley L. J., Groves B., Kauffmann G., Heckman T., The host galaxies and classification of active galactic nuclei, MNRAS, 2006, vol. 372, p. 961

Kimbro E., Reines A. E., Molina M., Deller A. T., Stern D., Clumpy Star Formation and AGN Activity in the Dwarf–Dwarf Galaxy Merger Mrk 709, The Astrophysical Journal, 2021, vol. 912, p. 89

King A., Pounds K., Powerful Outflows and Feedback from Active Galactic Nuclei, Annual Review of Astronomy and Astrophysics, 2015, vol. 53, p. 115

Kirby E. N., Simon J. D., Geha M., Guhathakurta P., Frebel A., Uncovering Extremely Metal-Poor Stars in the Milky Way's Ultrafaint Dwarf Spheroidal Satellite Galaxies, ApJ, 2008, vol. 685, p. L43

Klypin A., Kravtsov A. V., Valenzuela O., Prada F., Where Are the Missing Galactic Satellites?, ApJ, 1999, vol. 522, p. 82

Kormendy J., Families of ellipsoidal stellar systems and the formation of dwarf elliptical galaxies., ApJ, 1985, vol. 295, p. 73

Kornecki P., Pellizza L. J., del Palacio S., Müller A. L., Albacete-Colombo J. F., Romero G. E., γ-ray/infrared luminosity correlation of star-forming galaxies, A&A, 2020, vol. 641, p. A147

Koudmani S., Sijacki D., Bourne M. A., Smith M. C., Fast and energetic AGN-driven outflows in simulated dwarf galaxies, Monthly Notices of the Royal Astronomical Society, 2019, vol. 484, p. 2047

Kravtsov A., Dark Matter Substructure and Dwarf Galactic Satellites, Advances in Astronomy, 2010, vol. 2010, p. 1

Kunth D., Sargent W. L. W., Bothun G. D., A Dwarf Galaxy with Seyfert Characteristics, AJ, 1987, vol. 93, p. 29

Lamastra A., Extragalactic gamma-ray background from AGN winds and star-forming galaxies in cosmological galaxy-formation models, Astronomy &amp Astrophysics, 2017, vol. 607, p. A18

Lanfranchi G. A., Hazenfratz R., Caproni A., Silk J., Parameterizing the Outflow from a Central Black Hole in Dwarf Spheroidal Galaxies: A 3D Hydrodynamic Simulation, The Astrophysical Journal, 2021, vol. 914, p. 32

Larson R. B., Effects of Supernovae on the Early Evolution of Galaxies, Monthly Notices of the Royal Astronomical Society, 1974, vol. 169, p. 229

Lehmer B. D., THE EVOLUTION OF NORMAL GALAXY X-RAY EMISSION THROUGH COSMIC HISTORY: CONSTRAINTS FROM THE 6 MSiCHANDRA/iDEEP FIELD-SOUTH, The Astrophysical Journal, 2016, vol. 825, p. 7

Liang E. P., Nolan P. L., CYGNUS-X-1 Revisited, Space Sci. Rev., 1984, vol. 38, p. 353

Licquia T. C., Newman J. A., Improved Estimates of the Milky Way's Stellar Mass and Star Formation Rate from Hierarchical Bayesian Meta-Analysis, ApJ, 2015, vol. 806, p. 96

LIGO Collaboration V., Observation of Gravitational Waves from a Binary Black Hole Merger, Phys. Rev. Lett., 2016, vol. 116, p. 061102

Liu R.-Y., Murase K., Inoue S., Ge C., Wang X.-Y., Can Winds Driven by Active Galactic Nuclei Account for the Extragalactic Gamma-Ray and Neutrino Backgrounds?, The Astrophysical Journal, 2018, vol. 858, p. 9

Liu W., Veilleux S., Canalizo G., Rupke D. S. N., Manzano-King C. M., Bohn T., U V., Integral Field Spectroscopy of Fast Outflows in Dwarf Galaxies with AGNs, ApJ, 2020, vol. 905, p. 166

Ludwig R. R., Greene J. E., Barth A. J., Ho L. C., PHYSICAL PROPERTIES OF THE NARROW-LINE REGION OF LOW-MASS ACTIVE GALAXIES, The Astrophysical Journal, 2012, vol. 756, p. 51

Lynden-Bell D., Galactic Nuclei as Collapsed Old Quasars, Nature, 1969, vol. 223, p. 690

Lynds R., The Absorption-Line Spectrum of 4c 05.34, ApJ, 1971, vol. 164, p. L73

Ma L., Hopkins P. F., Seeds don't sink: even massive black hole âseedsâ cannot migrate to galaxy centres efficiently, Monthly Notices of the Royal Astronomical Society, 2021, vol. 508, p. 1973

Mahadevan R., Narayan R., Krolik J., Gamma-Ray Emission from Advection-dominated Accretion Flows around Black Holes: Application to the Galactic Center, The Astrophysical Journal, 1997, vol. 486, p. 268

Manzano-King C. M., Canalizo G., Active galactic nucleus and dwarf galaxy gas kinematics, Monthly Notices of the Royal Astronomical Society, 2020, vol. 498, p. 4562

Marconi G., Matteucci F., Tosi M., Element abundances in blue compact galaxies., MNRAS, 1994, vol. 270, p. 35

Martin N. F., de Jong J. T. A., Rix H.-W., A Comprehensive Maximum Likelihood Analysis of the Structural Properties of Faint Milky Way Satellites, The Astrophysical Journal, 2008, vol. 684, p. 1075

Massaro F., Thompson D. J., Ferrara E. C., The extragalactic gamma-ray sky in the Fermi era, The Astronomy and Astrophysics Review, 2015, vol. 24

Mateo M., DWARF GALAXIES OF THE LOCAL GROUP, Annual Review of Astronomy and Astrophysics, 1998, vol. 36, p. 435

Matteucci F., Chiosi C., Stochastic star formation and chemical evolution of dwarf irregular galaxies., A&A, 1983, vol. 123, p. 121

Matteucci F., Tosi M., Nitrogen and oxygen evolution in dwarf irregular galaxies, Monthly Notices of the Royal Astronomical Society, 1985, vol. 217, p. 391

Mattox J. R., The Likelihood Analysis of EGRET Data, ApJ, 1996, vol. 461, p. 396

Merloni A., Heinz S., Di Matteo T., A Fundamental Plane of black hole activity, Monthly Notices of the Royal Astronomical Society, 2003, vol. 345, p. 1057

Mezcua M., Feeding and feedback from little monsters: AGN in dwarf galaxies, Proceedings of the International Astronomical Union, 2019, vol. 15, p. 238

Mezcua M., Prieto M. A., EVIDENCE OF PARSEC-SCALE JETS IN LOW-LUMINOSITY ACTIVE GALACTIC NUCLEI, The Astrophysical Journal, 2014, vol. 787, p. 62

Mineo S., Gilfanov M., Sunyaev R., X-ray emission from star-forming galaxies â I. High-mass X-ray binaries, Monthly Notices of the Royal Astronomical Society, 2012, vol. 419, p. 2095

Molina M., Reines A. E., Greene J. E., Darling J., Condon J. J., Outflows, Shocks, and Coronal Line Emission in a Radio-selected AGN in a Dwarf Galaxy, The Astrophysical Journal, 2021, vol. 910, p. 5

Molina M., Reines A. E., Latimer C. J., Baldassare V., Salehirad S., A Sample of Massive Black Holes in Dwarf Galaxies Detected via [Fe X] Coronal Line Emission: Active Galactic Nuclei and/or Tidal Disruption Events, ApJ, 2021, vol. 922, p. 155

Moore B., Ghigna S., Governato F., Lake G., Quinn T., Stadel J., Tozzi P., Dark Matter Substructure within Galactic Halos, ApJ, 1999, vol. 524, p. L19

Mortlock D. J., A luminous quasar at a redshift of z = 7.085, Nature, 2011, vol. 474, p. 616

Müller-Sánchez F., Prieto M. A., Outflows from Active Galactic Nuclei: Kinematics of the Narrow-line and Coronal-line Regions in Seyfert Galaxies, ApJ, 2011, vol. 739, p. 69

Narayan R., Low-Luminosity Accretion in Black Hole X-Ray Binaries and Active Galactic Nuclei, Ap&SS, 2005, vol. 300, p. 177

Narayan R., McClintock J. E., Advection-dominated accretion and the black hole event horizon, New Astronomy Reviews, 2008, vol. 51, p. 733

Narayan R., Yi I., Advection-dominated Accretion: A Self-similar Solution, ApJ, 1994, vol. 428, p. L13

Negus J., Comerford J. M., SÃ¡nchez F. M., Barrera-Ballesteros J. K., Drory N., Rembold S. B., Riffel R. A., , 2021 The Physics of the Coronal Line Region for Galaxies in MaNGA

Nemmen R., Storchi-Bergmann T., Eracleous M., , 2011 Spectral Energy Distribution Models for Low-luminosity Active Galactic Nuclei in LINERs

Nemmen R. S., Georganopoulos M., Guiriec S., Meyer E. T., Gehrels N., Sambruna R. M., A Universal Scaling for the Energetics of Relativistic Jets from Black Hole Systems, Science, 2012, vol. 338, p. 1445

Nemmen R. S., Storchi-Bergmann T., Eracleous M., Spectral models for low-luminosity active galactic nuclei in LINERs: the role of advection-dominated accretion and jets, Monthly Notices of the Royal Astronomical Society, 2014, vol. 438, p. 2804

Nguyen D. D., Seth A. C., Neumayer N., Kamann S., Voggel K. T., Cappellari M., Picotti A., Nguyen P. M., Böker T., Debattista V., Caldwell N., McDermid R., Bastian N., Ahn C. C., Pechetti R., Nearby Early-type Galactic Nuclei at High Resolution: Dynamical Black Hole and Nuclear Star Cluster Mass Measurements, ApJ, 2018, vol. 858, p. 118

Nolan P. L., Fermi Large Area Telescope Second Source Catalog, ApJS, 2012, vol. 199, p. 31

Oetken L., An Equatorially Symmetric Rotator Model for Magnetic Stars, Astronomische Nachrichten, 1977, vol. 298, p. 197

Oka K., Manmoto T., Gamma-ray emission from an accretion flow around a Kerr black hole, Monthly Notices of the Royal Astronomical Society, 2003, vol. 340, p. 543

Oke J. B., Schmidt M., Optical Observations of the Radio Source 3C 273., AJ, 1963, vol. 68, p. 288

Osmer P. S., , 2003 The Evolution of Quasars

Paliya V. S., Domínguez A., Ajello M., Franckowiak A., Hartmann D., Fermi-LAT Stacking Analysis Technique: An Application to Extreme Blazars and Prospects for their CTA Detection, ApJ, 2019, vol. 882, p. L3

Peng F.-K., Zhang H.-M., Wang X.-Y., Wang J.-F., Zhi Q.-J., Evidence of AGN Activity in the Gamma-Ray Emission from Two Starburst Galaxies, ApJ, 2019, vol. 884, p. 91

Penston M. V., Fosbury R. A. E., Boksenberg A., Ward M. J., Wilson A. S., The Fe9+ region in active galactic nuclei, Monthly Notices of the Royal Astronomical Society, 1984, vol. 208, p. 347

Peterson B. M., , 2001 in , Advanced Lectures on the Starburst-AGN Connection. WORLD SCIENTIFIC pp 3–68

Peterson B. M., Multiwavelength Monitoring of the Dwarf Seyfert 1 Galaxy NGC 4395. I. A Reverberation-based Measurement of the Black Hole Mass, ApJ, 2005, vol. 632, p. 799

Prieto M. A., Viegas S. M., On the Ionizing Continuum in Active Galactic Nuclei: Clues from theiInfrared Space Observatory/i, The Astrophysical Journal, 2000, vol. 532, p. 238

Rawlings S., Saunders R., Evidence for a common central-engine mechanism in all extra-galactic radio sources, Nature, 1991, vol. 349, p. 138

Reeves J. N., O'Brien P. T., Ward M. J., A Massive X-Ray Outflow from the Quasar PDS 456, The Astrophysical Journal, 2003, vol. 593, p. L65

Reines A. E., Hunting for massive black holes in dwarf galaxies, Nature Astronomy, 2022, vol. 6, p. 26

Reines A. E., Condon J. J., Darling J., Greene J. E., A New Sample of (Wandering) Massive Black Holes in Dwarf Galaxies from High-resolution Radio Observations, ApJ, 2020, vol. 888, p. 36

Reines A. E., Greene J. E., Geha M., Dwarf Galaxies with Optical Signatures of Active Massive Black Holes, ApJ, 2013, vol. 775, p. 116

Richardson C. T., Optical and JWST Mid-IR Emission Line Diagnostics for Simultaneous IMBH and Stellar Excitation in z $\sim$ 0 Dwarf Galaxies$*$, $The Astrophysical Journal$, 2022, $vol.$ 927, $p.$165

Rodríguez-Ardila A., Fonseca-Faria M. A., A 700 pc Extended Coronal Gas Emission in the Circinus Galaxy, The Astrophysical Journal, 2020, vol. 895, p. L9

Rodriguez-Ardila A., Viegas S. M., Pastoriza M. G., Prato L., Near-Infrared Coronal Lines in Narrow-Line Seyfert 1 Galaxies, The Astrophysical Journal, 2002, vol. 579, p. 214

Salpeter E. E., Accretion of Interstellar Matter by Massive Objects., ApJ, 1964, vol. 140, p. 796

Salvadori S., Ferrara A., Schneider R., Life and times of dwarf spheroidal galaxies, MNRAS, 2008, vol. 386, p. 348

Sargent A. J., Johnson M. C., Reines A. E., Secrest N. J., van der Horst A. J., Cigan P. J., Darling J., Greene J. E., Wandering Black Hole Candidates in Dwarf Galaxies at VLBI Resolution, 2022

Schmidt M., 3C 273 : A Star-Like Object with Large Red-Shift, Nature, 1963, vol. 197, p. 1040

Schmidt M., Matthews T. A., Redshift of the Quasi-Stellar Radio Sources 3c 47 and 3c 147., ApJ, 1964, vol. 139, p. 781

Schmidt M., Schneider D. P., Gunn J. E., Spectrscopic CCD Surveys for Quasars at Large Redshift.IV.Evolution of the Luminosity Function from Quasars Detected by Their Lyman-Alpha Emission, AJ, 1995, vol. 110, p. 68

Schneider A., Trujillo-Gomez S., Papastergis E., Reed D. S., Lake G., Hints against the cold and collisionless nature of dark matter from the galaxy velocity function, Monthly Notices of the Royal Astronomical Society, 2017, vol. 470, p. 1542

Schombert J. M., Pildis R. A., Eder J. A., Oemler Augustus J., Dwarf Spirals, AJ, 1995, vol. 110, p. 2067

Seyfert C. K., Nuclear Emission in Spiral Nebulae., ApJ, 1943, vol. 97, p. 28

Shakura N. I., Sunyaev R. A., Black holes in binary systems. Observational appearance., A&A, 1973, vol. 24, p. 337

Silk J., Feedback by Massive Black Holes in Gas-rich Dwarf Galaxies, The Astrophysical Journal, 2017, vol. 839, p. L13

Smith N., CORONAL LINES AND DUST FORMATION IN SN 2005ip: NOT THE BRIGHTEST, BUT THE HOTTEST TYPE IIn SUPERNOVA, The Astrophysical Journal, 2009, vol. 695, p. 1334

Soltan A., Masses of quasars., MNRAS, 1982, vol. 200, p. 115

Stark D. P., Loeb A., Ellis R. S., An Empirically Calibrated Model for Interpreting the Evolution of Galaxies during the Reionization Era, The Astrophysical Journal, 2007, vol. 668, p. 627

Strong A. W., GLOBAL COSMIC-RAY-RELATED LUMINOSITY AND ENERGY BUDGET OF THE MILKY WAY, The Astrophysical Journal, 2010, vol. 722, p. L58

Takami H., γ-rays as a diagnostic of the origin of core radiation in low-luminosity active galactic nuclei, Monthly Notices of the Royal Astronomical Society, 2011, vol. 413, p. 1845

Tammann G. A., Dwarf Galaxies in the Past. In European Southern Observatory Conference and Workshop Proceedings , vol. 49 of European Southern Observatory Conference and Workshop Proceedings, 1994, p. 3

Tchekhovskoy A., Narayan R., McKinney J. C., BLACK HOLE SPIN AND THE RADIO LOUD/QUIET DICHOTOMY OF ACTIVE GALACTIC NUCLEI, The Astrophysical Journal, 2010, vol. 711, p. 50

Thompson D. J., Digel S. W., Racusin J. L., Exploring the extreme universe with the Fermi Gamma-Ray Space Telescope, Physics Today, 2012, vol. 65, p. 39

Thornton C. E., Barth A. J., Ho L. C., Rutledge R. E., Greene J. E., The Host Galaxy and Central Engine of the Dwarf Active Galactic Nucleus POX 52, The Astrophysical Journal, 2008, vol. 686, p. 892

Tolstoy E., Hill V., Tosi M., Star-Formation Histories, Abundances, and Kinematics of Dwarf Galaxies in the Local Group, Annual Review of Astronomy and Astrophysics, 2009, vol. 47, p. 371

Tombesi F., Sambruna R. M., Reeves J. N., Braito V., Ballo L., Gofford J., Cappi M., Mushotzky R. F., DISCOVERY OF ULTRA-FAST OUTFLOWS IN A SAMPLE OF BROAD-LINE RADIO GALAXIES OBSERVED WITHiSUZAKU/i, The Astrophysical Journal, 2010, vol. 719, p. 700

Tremonti C. A., Heckman T. M., Kauffmann G., Brinchmann J., Charlot S., White S. D. M., Seibert M., Peng E. W., Schlegel D. J., Uomoto A., Fukugita M., Brinkmann J., The Origin of the Mass-Metallicity Relation: Insights from 53,000 Star-forming Galaxies in the Sloan Digital Sky Survey, ApJ, 2004, vol. 613, p. 898

van Dokkum P. G., Abraham R., Merritt A., Zhang J., Geha M., Conroy C., FORTY-SEVEN MILKY WAY-SIZED, EXTREMELY DIFFUSE GALAXIES IN THE COMA CLUSTER, The Astrophysical Journal, 2015, vol. 798, p. L45

Veilleux S., A Study of the Structure and Kinematics of the Narrow-Line Region in Seyfert Galaxies. II. Analysis of the Line-Profile Parameters, ApJS, 1991, vol. 75, p. 383

Veilleux S., Osterbrock D. E., Spectral Classification of Emission-Line Galaxies, ApJS, 1987, vol. 63, p. 295

Volonteri M., Lodato G., Natarajan P., The evolution of massive black hole seeds, MNRAS, 2008, vol. 383, p. 1079

Wang X., Loeb A., Contribution of quasar-driven outflows to the extragalactic gamma-ray background, Nature Physics, 2016, vol. 12, p. 1116

Wang X., Loeb A., Cumulative neutrino background from quasar-driven outflows, Journal of Cosmology and Astroparticle Physics, 2016, vol. 2016, p. 012

Wang X., Loeb A., Ultrahigh energy cosmic rays from nonrelativistic quasar outflows, Physical Review D, 2017, vol. 95

Weinberg D. H., The Lyman- Forest as a Cosmological Tool. In AIP Conference Proceedings , AIP, 2003

Yang Y., Wilson A. S., Matt G., Terashima Y., Greenhill L. J., Suzaku Observations of the Circinus Galaxy, ApJ, 2009, vol. 691, p. 131

Yaqoob T., The nature of the Compton-thick X-ray reprocessor in NGC 4945, MNRAS, 2012, vol. 423, p. 3360

York D. G., The Sloan Digital Sky Survey: Technical Summary, AJ, 2000, vol. 120, p. 1579

Yuan F., Narayan R., Hot Accretion Flows Around Black Holes, Annual Review of Astronomy and Astrophysics, 2014, vol. 52, p. 529

Zavala J., THE VELOCITY FUNCTION IN THE LOCAL ENVIRONMENT FROM ΛCDM AND ΛWDM CONSTRAINED SIMULATIONS, The Astrophysical Journal, 2009, vol. 700, p. 1779

Zel'dovich Y. B., Novikov I. D., Estimating the mass of a super-star, Dokl. Akad. Nauk SSSR, 1964, vol. 158, p. 811